PSFC/JA-04-17

Transport-Driven Scrape-Off Layer Flows and the Boundary Conditions Imposed at the Magnetic Separatrix in a Tokamak Plasma

B. LaBombard*, J.E. Rice, A.E. Hubbard, J.W. Hughes,
M. Greenwald, J. Irby, Y. Lin, B. Lipschultz, E.S. Marmar,
C.S. Pitcher,† N. Smick, S.M. Wolfe, S.J. Wukitch, and the
Alcator Group

11 May 2004

Plasma Science and Fusion Center
Massachusetts Institute of Technology
Cambridge, MA 02139 USA

*Tel.: 617-253-7264, Fax: 1-617-253-0627: e-mail: labombard@psfc.mit.edu
†presently at 132 Boxwood Ave., Toronto, Canada M4N1Y5

This work was supported by the U.S. Department of Energy, Cooperative Grant No. DE-FC02-99ER54512.

Submitted for publication to *Nuclear Fusion*.

Transport-Driven Scrape-off Layer Flows and the Boundary Conditions Imposed at the Magnetic Separatrix in a Tokamak Plasma

B. LaBombard,* J.E. Rice, A.E. Hubbard, J.W. Hughes,
M. Greenwald, J. Irby, Y. Lin, B. Lipschultz, E.S. Marmar, C.S. Pitcher,†
N. Smick, S.M. Wolfe, S.J. Wukitch,
and the Alcator Group

Massachusetts Institute of Technology, Plasma Science and Fusion Center,
175 Albany St., Cambridge, MA 02139 USA

Plasma profiles and flows in the low- and high-field side scrape-off layer (SOL) regions in Alcator C-Mod are found to be remarkably sensitive to magnetic separatrix topologies (upper-, lower-, and double-null) and to impose topology-dependent flow boundary conditions on the confined plasma. Near-sonic plasma flows along magnetic field lines are observed in the high-field SOL with magnitude and direction clearly dependent on x-point location. The principal drive mechanism for the flows is a strong ballooning-like poloidal transport asymmetry: parallel flows arise so as to re-symmetrize the resulting poloidal pressure variation in the SOL. Additionally, the decrease in cross-sectional area of a magnetic flux tube connecting from low to high-field regions appears to act as a 'nozzle', increasing flow velocities in the high-field SOL. Secondary flows involving a combination of toroidal rotation and Pfirsch-Schlüter ion currents are also evident. As a result of the transport-driven parallel flows, the SOL exhibits a net co-current (counter-current) volume-averaged toroidal momentum when $B \times \nabla B$ is toward (away from) the x-point. Depending on discharge conditions, flow momentum can couple across the separatrix and affect the toroidal rotation of the confined plasma. This mechanism accounts for a positive (negative) increment in central plasma co-rotation seen in L-mode discharges when $B \times \nabla B$ is toward (away from) the x-point. Experiments suggest that topology-dependent flow boundary conditions may also play a role in the sensitivity of L-H power threshold to x-point location: in a set of otherwise similar discharges, the L-H transition is seen to be coincident with central rotation achieving roughly the same value, *independent* of magnetic topology. For discharges with $B \times \nabla B$ pointing away from the x-point (i.e., with the SOL flow boundary condition *impeding* co-current rotation), the same characteristic rotation can only be achieved with *higher* input power.

PACS: 52.30.-q, 52.25.Fi, 52.25.Gj, 52.40.Hf, 52.55.Fa, 52.70.Ds, 52.70.Nc

---

*Tel.: 1-617-253-7264, Fax: 1-617-253-0627: e-mail: labombard@psfc.mit.edu.
†presently at 132 Boxwood Ave., Toronto, Canada M4N1Y5.

1. Introduction

Plasma flow along magnetic field lines has been measured in the scrape-off layer (SOL) of many tokamaks [1-12], with velocities approaching a significant fraction of the local sound speed. While such strong flows are expected on field lines near to a material surface, these flows are found in regions far from any surface. The physical mechanism(s) behind such flows is an active area of research, since, depending on the drive mechanisms and resultant total velocity vectors, these flows may affect the impurity compression of the divertor, the transport of impurities in the SOL plasma, and perhaps the balance of material erosion and redeposition between the inner and outer divertor legs, all of which can impact future reactor devices such as ITER [13].

A number of mechanisms is known to yield parallel flows in the SOL: ionization imbalances, Pfirsch-Schlüter flows, poloidal transport asymmetries (e.g., ballooning-like transport), and toroidal rotation. Analytic models and numerical simulations [8, 9, 14-18] have investigated such effects with the goal of reproducing observed flows and assessing their impact on impurity distributions. While in some cases models have produced flows similar to measurement (e.g., JT-60U [19]), there are other cases where the measured flows appear too large (e.g., JET [9]). One difficulty is the complexity of the flow pattern. Parallel flows measured near material surfaces (e.g., in the divertor) are largely independent of those far away [10] which in turn may have spatial variation. In this regard, multipoint flow measurements far from the divertor are desired but rarely available.

Despite large differences in first-wall and divertor geometries between experimental devices, parallel flows measured at locations far from material surfaces exhibit remarkably similar characteristics. In diverted discharges, there is a tendency for the plasma to flow along field lines in the co-current direction near the separatrix. This is seen at locations 'upstream' of the outer divertor (JT-60U [8], C-Mod [7]), near the outer midplane (TCV [12], C-Mod [7]), and near the top of the poloidal cross-section (JET [9]). These flows tend to reverse (although sometimes not symmetrically) when the magnetic field is reversed. In JT-60U, only slight perturbations to the

parallel flows (< ~20%) were seen during conditions of strong gas-injection and divertor pumping [20] – evidence that these flows are dominated by effects other than ionization and fueling imbalances.

In retrospect, measurements of SOL flows in limiter discharges (Alcator C [1], T-10[2], DITE [4]) also exhibited many features seen in diverted discharges. The drive mechanisms for these were associated with a combination of ballooning-like cross-field transport asymmetries [21] and co-current toroidal rotation. Co-current rotation is a natural consequence of the positive radial electric field that exists on open field lines in the SOL [22]; it is a divergence-free $\underline{E} \times \underline{B}$ motion ($V_\phi = E_r / B_\theta, V_\theta = 0$), incurring minimal resistance in the axisymmetric geometry. Results from divertor biasing experiments in TdeV clearly demonstrated this effect [6]: in response to an applied radial electric field, the SOL plasma simply rotated toroidally. Ballooning-like cross-field transport is a more intractable mechanism; since there is no theoretical prescription for the magnitude and poloidal distribution of plasma turbulence and associated cross-field transport, it remains a free parameter in models. In fact, in circumstances where parallel flows are dominated by ballooning-like transport asymmetries, a direct measurement of such *transport-driven flows* can reveal key missing information about the underlying plasma turbulence and transport.

Another potentially important aspect of the SOL flows, which has been largely overlooked, is the effect that they might have on the core plasma. Do these experimentally observed SOL flows influence the boundary conditions on the confined plasma in any significant way? Measurements of central plasma toroidal rotation in Alcator C-Mod have uncovered clear connections between the rotation profile and the operation of the tokamak in a variety of energy confinement modes [23]. It is important to note that these observations were made in ion-cyclotron range-of-frequency (ICRF) heated discharges, with no external source of momentum input – a situation that is expected in a reactor-scale device such as ITER. Immediately after an L-H transition, a prompt increase in co-current rotation is seen, starting near the edge and propagating into the plasma center over timescales on the order of the energy confinement time [24] – clear evidence that flow conditions

near the edge influence central plasma rotation. Interestingly, the central rotation speed in ohmic L-mode was found to depend on the magnetic topology, favoring stronger counter-current rotation in upper versus lower x-point discharges with otherwise similar conditions ($B \times \nabla B$ directed downward) [23]. Since these plasmas had no external toroidal momentum input, the key difference must be associated with the boundary conditions imposed on the confined plasma, e.g., the toroidal projection of the plasma flows near the separatrix in the SOL.

This paper addresses both aspects of plasma flows on Alcator C-Mod from an experimental point of view: (1) the observed SOL flow pattern and principal drive mechanisms responsible and (2) the resultant toroidal flow boundary conditions seen by the confined plasma at the separatrix. Our investigation is based on new plasma profile and flow information from scanning probes located in both the high- and low-field scrape-off layer regions as well as core plasma rotation measurements. The research has revealed a rich interplay among anomalous cross-field transport, strong plasma flow along magnetic field lines, magnetic topology and toroidal rotation in the edge plasma. In particular, remarkably rapid plasma flows parallel to magnetic field lines are observed in the high-field SOL. Their origins are traced to a strong ballooning-like component to the cross-field transport, which is particularly manifest in a comparison of high and low-field side SOL profiles in near double-null discharges. We have also found that the SOL plasma flows do indeed impose influential boundary conditions on the confined plasma: setting the toroidal rotation of the plasma near the separatrix and, as a result, affecting the toroidal rotation of the plasma as a whole. Moreover, our research suggests that topology-dependent SOL flow boundary conditions may offer an explanation for the dependence of the L-H power threshold on x-point location: in a set of otherwise similar discharges, the L-H transition is observed to coincide with co-current plasma rotation achieving roughly the same value in both upper and lower-null topologies (with $B \times \nabla B$ down). However, in upper-null, the SOL flow boundary condition *impedes* co-current plasma rotation. Correspondingly, higher input power (which in itself tends to spin the plasma in the co-current direction through an increase in stored plasma energy [25]) is seen necessary to attain H-

mode in this topology.

Section 2 briefly outlines the key plasma flow diagnostics for this study: a magnetically-driven fast-scanning swing-probe near the midplane on the high-field SOL [26], two scanning-Mach probes on the low-field SOL [11] and core plasma rotation inferred from the Doppler-shifts of central Ar^{17+} ions [23]. Section 3 reports results from a set of experiments aimed at sorting out the principal drive mechanisms responsible for the observed SOL flows. These data reveal three flow components: a strong flow along magnetic field lines from the low- to high-field SOL, toroidal plasma rotation and Pfirsch-Schlüter flow. In addition, data from different magnetic topologies (lower x-point, upper x-point, double-null) indicate that a ballooning-like component to the cross-field plasma transport is the underlying cause for the strong parallel flow - in single-null topologies, plasma exists on the high field side SOL *principally because it flows along field lines from the low-field side*.

A simple flux-tube model of plasma flows is presented in Section 4. Data from upper and lower-null discharges (with $B \times \nabla B$ down) are combined to extract just the transport-driven, parallel component of the plasma flow. An estimate of the net particle source profile along flux tubes is constructed, elucidating the ballooning-like asymmetry of the cross-field particle transport and yielding rough estimates for effective particle transport velocity (V_{eff}) and diffusion (D_{eff}) coefficients. This data-constrained model also clearly illustrates how the SOL can possess a net volume-averaged co-current (counter-current) toroidal momentum when the $B \times \nabla B$ direction is towards (away from) the x-point.

Section 5 examines connections between plasma flows near the separatrix and in the plasma center. A clear correspondence is noted, demonstrating that the topology-dependent SOL flows set flow boundary conditions for the confined plasma and affect the radial electric fields near the separatrix. Finally, a set of experimental observations is presented in section 6 that suggests magnetic topology, SOL flows, toroidal rotation and the dependence of the L-H power threshold on x-point location are fundamentally connected. Concluding remarks are contained in section 7.

2. Experiment and flow diagnostics

Background information on Alcator C-Mod's design, diagnostics and operational characteristics can be found in reference [27]. A cross-section of a typical Alcator C-Mod equilibrium used for the present study and locations of key plasma flow diagnostics are shown in Fig. 1. The results reported in this paper were obtained from a variety of ohmic heated deuterium discharges, including plasma currents (I_p) between 0.5 and 1.0 MA, toroidal magnetic field strength (B_T) between 4 and 6 tesla and line-averaged plasma densities, $0.8 < \overline{n}_e < 2.4$ x10^{20} m^{-3} plus some ICRF heated discharges (discussed further in section 6) that exhibited an L-H transition. The influence of magnetic topology (i.e., upper-, lower-, and double-null) on plasma conditions was studied by fixing the direction of toroidal magnetic field and plasma current in the 'normal' direction (B_T and I_p aligned, $B \times \nabla B$ pointing down) and changing the magnetic flux balance between upper and lower x-points. The effect of reversing the directions of B_T and I_p was studied for a subset of discharges (section 3.3). In this case, the magnetic topology was fixed in lower single-null, similar to that shown in Fig. 1.

Views of the outer scanning probe, located 11 cm above the midplane on the large major radius side of the torus, are shown in Fig. 1. The EAST and WEST tungsten electrodes, which are embedded in an electrically floating molybdenum body, sample plasma from opposite directions along the same field line, forming a 'Mach probe pair' in which the parallel Mach number can be estimated from the ratio of ion saturation current densities, $M_{//} = 0.43\, ln\left(J_{east} / J_{west}\right)$ [28]. By fitting positive and negative-going *I-V* characteristics from the EAST and WEST electrodes, electron densities (n), temperatures (T_e) and parallel Mach numbers ($M_{//}$) along the probe's trajectory are obtained every 0.25 ms (corresponding to ~0.25 mm of probe travel). The NORTH and SOUTH tungsten electrodes were operated in a floating-voltage mode (1 MHz sample frequency). These electrodes are used to estimate the poloidal phase velocity of plasma fluctuations.

The vertical scanning probe (location shown in Fig. 1) is of similar construction [29] and is operated in the same manner.

The inner scanning probe, which is located 5.8 cm above the midplane on the small major radius side of the torus (Fig. 1), consists of a single tungsten electrode embedded in an electrically isolated carbon fiber composite graphite body and aligned flush with the surface of a short cylindrical arm which extends from the body. Its novel electromechanical actuation is based on the divertor bypass flaps designed by Pitcher [30]. In response to a voltage waveform applied to an embedded coil, the probe body swings into the high-field side scrape-off layer, completing a 180-degree spin about its pivot axis. For angles less than 90 degrees, the flush-mounted electrode samples plasma in one direction along a field line while for angles greater than 90 degrees it samples the other. The single electrode is biased with respect to the graphite body with a swept-voltage waveform. In a manner similar to the other scanning probes, cross-field profiles of density, temperature and parallel Mach number are assembled. However, in this case the Mach number is computed from the ratio of the ion saturation current densities when the probe is looking 'upstream' versus 'downstream' along magnetic field lines. Owing to geometrical inaccuracies and concerns about interpreting probe data when field lines are nearly tangent to the electrode surface [31], data collected for pivot angles between ~80 and ~100 degrees are excluded from the analysis.

The three probes are typically operated together, simultaneously executing two or three scans during a single discharge. The resultant data are mapped onto magnetic flux surfaces reconstructed from magnetic measurements [32] and the EFIT plasma equilibrium code [33]. The flux-surface coordinate used here, ρ, is defined as the distance into the SOL along a major radius at the outer midplane. Small shifts in the ρ-axis (up to 2 mm) have been applied to some probe data, using SOL power balance as a constraint.

X ray spectra along a toroidal line of sight tangent to the plasma center (R = 0.685 m) are recorded using a fixed von Hamos type crystal X ray spectrometer [23]. Central toroidal rotation velocities of Ar^{17+} ions are inferred from the Doppler shifts of the corresponding Ly_α doublet.

Trace amounts of argon are injected early in the discharge to facilitate the measurement. This technique avoids the use of neutral beams, which can add toroidal momentum to the plasma and perturb intrinsic self-generated flows. Owing to the high charge state of the argon ions, their toroidal rotation is expected to be well coupled and close to the toroidal rotation of the plasma background. This hypothesis is supported by an independent inference of toroidal plasma rotation through sawtooth oscillations [34, 35].

3. Scrape-off layer profiles and flows

The scanning probes have yielded a wealth of information on cross-field plasma profiles, including plasma flow, and their sensitivities to magnetic topology and discharge conditions. First, we compare inner and outer data from a set of three representative plasmas where only the x-point topology was changed: lower-single null (LSN), upper-single-null (USN), and near double null (DN). We then examine the effect of changing plasma density (section 3.2) followed by a compilation of information on poloidal plasma flows (section 3.3).

3.1. Effect of magnetic topology

The magnetic equilibria and probe-inferred plasma profile data for representative LSN, USN and DN discharges are shown in Figs. 2-4. These were ohmic L-mode plasmas (I_p= 0.78 MA, B_T=5.4 tesla, $\overline{n}_e$ = 1.4x10^{20} m^{-3}) with B_T and I_p aligned and $B \times \nabla B$ pointing down. The color-coded profiles (red – inner SOL, blue – outer) are smooth spline curves, fitted to data points recorded over the probes' trajectories. Typical ρ-spacings between individual data points were under 0.5 mm. The location of the magnetic separatrix ($\rho = 0$) is indicated, as well as locations that map to limiter surfaces. Data panels on the left show separate profiles recorded by "facing up" and "facing down" probes. A "facing up" ("facing down") probe collects plasma from field lines immediately connected to regions vertically above (below) the probe in the cross-sectional views of Figs. 2-4. Thus, the EAST electrode on the outer probe continuously records data "facing up" while the WEST records "facing down". The inner probe collects data from the "facing up"

direction when its pivot angle is less than 90 degrees; otherwise it collects data from the "facing down" direction.

A description of the quantities plotted in Figs. 2-4 follows:

Density, electron temperature, floating potential - These are standard quantities from magnetized probe theory [36], derived separately for the "facing up" and "facing down" electrodes. No correction is applied to account for background plasma flow; the densities reported here are those that would be expected in the ambient plasma with no flow present. The variation of the inner probe's projected area during its motion is taken into account. However, it should be noted that owing to non-ideal geometry and large clearances between electrode and probe body, the accuracy of the area estimate is uncertain (perhaps a ±50% error). Therefore, factors of ~2 differences in density (or electron pressure) between inner and outer profiles are possibly within systematic errors.

J_{sat} *fluctuations* – The quantity shown is the RMS ion saturation current fluctuation about the mean divided by the mean value. It is computed during the time interval when the probe's *I-V* characteristic is in the ion saturation regime, approximately a 200 μs time window. Thus, it is a measure of relative turbulence amplitude, derived from the fluctuation power spectrum above ~5 kHz.

Electron pressure – the average of nT_e for the "facing down" and "facing up" electrodes. This is a good first estimate of the ambient electron pressure, regardless of the background plasma flow speed.

Current ratio – is the ratio of local ion saturation current densities looking "upstream" and "downstream" along field lines. A ratio greater than one corresponds to flow in the co-current direction.

Mach number – This is computed using the Hutchinson formulation [28]. The formulation assumes the ratio of particle to momentum diffusivities to be unity; varying this ratio by a factor of

two can lead to a 20% variation in the inferred $M_{//}$. In addition, the theory is based on a uniform electron temperature; yet, significant electron temperature differences are evident on the "facing up" versus "facing down" electrodes (inner probe), which may introduce further errors. Positive $M_{//}$ correspond to flow in the co-current direction.

Toroidal projection of parallel velocity – is the quantity $V_{//\phi} = M_{//} C_s B_\phi / B$, where C_s is the local sound speed (assuming $T_i = T_e$) and B_ϕ / B is the local ratio of toroidal to total magnetic field strength. Positive $V_{//\phi}$ is in the co-current direction.

Focusing on Figs. 2 and 3, a number of important observations can be made:

(1) In both topologies, electron pressure roughly maps along field lines that connect between the inner and outer SOL. However, up/down averaged T_e are systematically lower in the inner SOL while up/down averaged n are higher. This is particularly evident at locations far from the separatrix, $\rho \sim 7$ mm.

(2) The inner probe detects different T_e values (by as much as a factor of ~2), depending on whether it is "facing up" or "facing down". Comparing the LSN and USN data, one can see that the lower T_e values are recorded when the probe faces toward the inner divertor strike-point, independent of topology.

(3) Normalized J_{sat} fluctuation levels are a factor of 3 to 10 lower in the inner SOL compared to outer – and this is on field lines that connect between the two. Note that much of the up/down variation in this quantity on the inner SOL can be explained by the up/down variation in the mean current collected by the probe. However, inner/outer differences in normalized J_{sat} fluctuation levels cannot be explained by variation in the means; factors of ~3 differences in absolute J_{sat} fluctuation levels are implied.

(4) Large current ratios (> 10 for LSN, < 0.1 for USN) and parallel mach numbers ($|M_{//}| \sim 1$)

are seen in the inner SOL. The measurements imply a co-current $V_{//\phi}$ in LSN and counter-current $V_{//\phi}$ in USN that has near-sonic speed near $\rho \sim 7$ mm. Near the separatrix, $V_{//\phi}$ does not symmetrically reverse in going from LSN to USN; the data appear to reflect about a counter-current offset of $M_{//} \sim -0.3$.

(5) The magnitudes of $M_{//}$ and $V_{//\phi}$ in the outer SOL are much smaller, changing from co-current values of $M_{//} < \sim 0.3$ in LSN to near zero or slightly negative values near the separatrix in USN.

Observations (1) and (2) are strong evidence for a poloidally asymmetric transport mechanism (ballooning-like) which preferentially exhausts plasma energy into the low-field (outer) SOL region. Apparently, T_e gradients arise so as to transport some of this power to the inner SOL region. The poloidal asymmetry in turbulence level inferred from (3) supports this picture. Similar asymmetries observed in inner/outer D_α fluctuation levels corroborate these measurements [37]. Observation (4) implies that particle exhaust is also poloidally asymmetric. The strong parallel plasma flows on the inner SOL and their topology-dependence may be simply interpreted as the plasma 'filling-in' the inner SOL by parallel flow; excess particles that spill into the outer SOL stream along field lines into the inner SOL. Flow features in (4) and (5) which do not symmetrically reverse in going from LSN to USN may involve a combination of toroidal rotation and/or Pfirsch-Schlüter currents. (Differences in the upper/lower divertor geometry or inaccuracies in the 'facing up" versus "facing down" probe areas could also play a role.)

Results from a DN discharge are shown in Fig. 4. Except for magnetic topology, this discharge was a match in all respects to the LSN and USN discharges. Important observations are:

(6) The inner T_e and n profiles are dramatically sharpened in DN discharges; the resultant electrons pressure e-folding lengths exhibit a factor of ~4 in/out asymmetry.

(7) In contrast to LSN and USN discharges, the inner probe detects no difference in T_e values when it is "facing up" versus "facing down".

(8) Normalized J_{sat} fluctuation levels remain a factor of ~2 lower on the inner SOL. Accounting for the reduction in the mean ion saturation current level, absolute J_{sat} fluctuations are an order of magnitude or more lower in the inner versus outer SOL.

(9) The magnitude of $V_{//\phi}$ on the inner SOL is greatly reduced compared to LSN and USN.

(10) The outer $V_{//\phi}$ profile does not go to zero. It exhibits values that are intermediate between LSN and USN.

The most compelling evidence for the existence of a strong ballooning-like transport mechanism is (6) which is augmented by (8). Further supporting evidence comes from recent D_α camera measurements [38]: For discharges in which the magnetic flux balance is swept in time from LSN to USN, the region of sharp e-folding length in the high-field SOL is seen to track with the secondary separatrix. Observation (7) is somewhat expected. But, most importantly, it tells us that the up/down T_e differences seen in LSN and USN discharges, (2), should be taken seriously. In light of all the other observations, (9) now comes completely expected; without a connection between the inner and outer SOL along field lines, the mechanism that drives strong parallel flow is absent. The residual parallel flow, (10), near the outer midplane in this up/down symmetric topology is interesting and suggestive of toroidal rotation and/or Pfirsch-Schlüter ion flow effects.

3.2. Effect of plasma density

Profiles and flows from a large set of discharges were collected to gain better statistics and to examine the effect of changing line-averaged density. A compilation of electron pressures (up/down averaged), normalized J_{sat} fluctuations and $V_{//\phi}$ profiles from 112 simultaneous probe scans in 44 discharges is shown in Fig. 5. Discharge conditions were: $I_p = 0.78$ MA, $B_T = 5.4$ tesla,

$\overline{n}_e$ ranging from 0.88 to 2.2x10^{20} m^{-3} in LSN, USN and DN topologies (magnetic equilibria identical to those in Figs. 2-4). The data are binned into three line-averaged density categories, $\overline{n}_e$ = 1.0, 1.5, 2.0x10^{20} m^{-3} and color-coded according to magnetic topology. Vertical bars indicate ±1 standard deviation, computed from the sample variance.

Figure 5 demonstrates that features seen in the individual discharges of Figs. 2-3 are robustly reproducible and persistent over the full range of densities: sharp in/out pressure gradient asymmetries in double null, lower fluctuation levels on inner SOL, strong (near-sonic) parallel plasma flow on inner SOL with direction clearly dependent on magnetic topology. The combined data set also yields a lower electron pressure on the inner SOL relative to outer, with separatrix values being the lowest in USN. The inner and outer electron pressure profiles clearly flatten with increasing density – a trend that has been well documented for outer SOL data [39]. Concurrently, we see the magnitude of $V_{//\phi}$ in the outer SOL decreasing with increasing $\overline{n}_e$. If we examine profiles at the vertical probe location for the same set of discharges (Fig. 6), we see a similar trend of flattened pressure profiles and reduced magnitude of $V_{//\phi}$ with increasing $\overline{n}_e$, although the $V_{//\phi}$ profile tends to peak near the separatrix at low densities.

In order to examine the density dependence in more detail, $V_{//\phi}$ at ρ = 4 mm measured by the three probes are plotted versus $\overline{n}_e$ in Fig. 7. The flows in the inner SOL clearly behave differently than in the outer SOL: the magnitude and direction of inner $V_{//\phi}$ is insensitive to $\overline{n}_e$ and appears to be affected by topology alone. In contrast, the direction of $V_{//\phi}$ at the outer probe location is persistently co-current at low densities. Its magnitude is affected by a topology change but not its direction. As density increases, the flow magnitude and its sensitivity to topology also decreases.

Flows detected at the vertical probe location are generally weaker and show less sensitivity to plasma density. Yet, nearer to the separatrix (Fig. 6) they recover the same trend as at the outer

probe location. The weaker co-current flows detected by this probe in LSN and DN discharges may be partly an artifact of this probe's presheath extending close to the lower divertor surface at large ρ (note the probe's proximity to the divertor in Fig.1). Indeed, recent analysis of C^{+2} impurity "plumes" at this location (generated via C_2D_4 gas injection) [40] suggests such an effect to be present, which would cause this Mach probe to report a counter-current offset to the true value of $V_{//\phi}$. The LSN data in Fig. 6 show a systematic decrease in $V_{//\phi}$ with ρ when $\rho > \sim 5$ mm, which is consistent with such an effect.

3.3. Poloidal flow information

As illustrated in Fig. 8, the Mach probes only detect the parallel component of total plasma flow, $V_{//total}$. This flow may consist of a combination of Pfirsch-Schlüter ion currents, $V_{//ps}$, toroidal plasma rotation, $V_{//rot}$, and a parallel component driven by cross-field transport, $V_{//trans}$, arising to satisfy particle balance. Ionization-driven parallel flow may also be considered, although its relative contribution to the observed flow magnitude is expected to be small at locations far from the divertor [17]. Moreover, during 'puff and pump' experiments in JT-60U [20], which were designed to maximally affect flows in the SOL, only a 20% change or less in the measured parallel flow speeds were seen. Note that depending on the cross-field component ($\underline{E}_r \times \underline{B}$ flow), a strong parallel flow could be just the manifestation of a strong toroidal plasma rotation, $V_{\phi rot} \sim E_r / B_\theta$. In this case, there could be little of no net poloidal particle flux. Should this be happening on the inner SOL, our inference of strong parallel flows being driven by cross-field transport asymmetries would be incorrect. In the following subsections, we assemble information on poloidal flows in the C-Mod SOL with an eye towards reconstructing the total flow pattern.

3.3.1 Impurity plumes

In a series of experiments aimed at studying flows near limiter and divertor surfaces, gaseous impurities were injected and low charge states of the resultant impurity "plumes" were imaged using a CCD camera with appropriate bandpass filters [41]. As shown by the representative

C^{+1} plumes in Fig. 9, the dispersion indicated a strong plasma flow and a clear dependence on x-point location, matching the flow behavior seen in Fig. 5. Moreover, with discharge conditions and LSN/USN equilibria very similar to data in Fig. 5, the strong flow was found to be persistently directed towards the inner divertor strike-point, independent of discharge density and independent of the direction of I_p and B_T (which were reversed together). Unfortunately, the impurity gas injection rate used in these experiments was large enough to perturb locally the plasma conditions, excluding a reliable estimate of the local plasma flow velocity from the impurity dispersal. However, the pattern does show the total flow vector to be closely aligned with the local magnetic field. Thus, the plumes provide strong evidence for parallel flows dominating over toroidal flows in the inner SOL. Additionally, the plumes clearly illustrate the effect of SOL flows on impurity migration: impurities born at the inside midplane wall migrate toward the inner divertor strike point, regardless of single-null x-point location.

3.3.2 Effect of reversed B

In contrast to the inner SOL, data in Fig. 5 suggest that $V_{//\phi}$ in the outer SOL are more indicative of toroidal rotation and/or Pfirsch-Schlüter flows; $V_{//\phi}$ there are less sensitive to x-point geometry and persistently co-current directed at low densities. In order to examine this trend further, electron pressure and parallel Mach number profiles from a series of matched LSN discharges ($0.5 < I_p < 1.0$ MA, $4 < B_T < 6$ tesla, $0.8 < \overline{n}_e < 2.4$ x10^{20} m^{-3}) with forward and reversed magnetic fields are shown in Fig. 10. Under the assumption that transport-driven parallel flows do not change, a comparison of forward and reversed-field discharges uncovers the contributions from toroidal rotation and/or Pfirsch-Schlüter flows (Fig. 8). Profile data are binned and color-coded according to discharge density normalized to Greenwald density [42], n/n_G, a parameter which is found to correlate with the character of transport and the behavior of profiles in the plasma edge [39]. Positive (negative) Mach numbers in the "normal *B*" ("reversed *B*") case indicate a co-current $V_{//\phi}$. In response to field reversal, $V_{//\phi}$ exhibits a roughly symmetric reversal

near the outer midplane, suggesting that the relative contribution of $V_{// trans}$ to the total flow is small. There are some differences however, which may relate to differences also seen in the electron pressure profiles (e.g., via changes in Pfirsch-Schlüter ion flows which are proportional to ion pressure gradients).

3.3.3 Radial electric fields

In principle, the radial electric field, E_r, can be estimated from the probe-inferred plasma potential profile, Φ_{ps}, and the resultant $\underline{E}_r \times \underline{B}$ component of plasma flow directly computed. This method involves adding an estimate of the sheath potential drop (~$2.8T_e$) to the probe's floating potential [43]. However, we have found inconsistencies between E_r inferred from this method and from two other methods: the poloidal propagation of plasma fluctuations [11] and the dispersal of impurity ions from a local gas puff [40]. These inconsistencies may be specific to our probe construction and/or the conditions found in C-Mod but likely involve plasma-surface effects, particularly those that influence secondary electron emission (affecting floating potentials and sheath potential drops). An additional complication, which is evident in the data of Figs. 2-4, is that a probe's floating potential depends on whether it is "facing up" or "facing down". While such an effect is expected in a flowing plasma, the ambiguity further brings into question the accuracy of E_r computed from these quantities, particularly since it involves taking the spatial gradient.

In view of these uncertainties, we treat Φ_{ps} as providing only qualitative information and avoid computing E_r from this quantity since the inferred magnitude (and even sign) could be wrong! However, it is reasonable to consider that as long as conditions near a probe (n, T_e, $|M_{//}|$) remain approximately the same, a change in Φ_{ps} arising from a change in topology should mimic the change in true Φ. With these ideas in mind, we plot Φ_{ps} profiles from the three probes in Fig. 11. The discharges correspond to those of Fig. 5 and a similar binning of the data has been performed. The algebraic average of the up/down floating potentials is used (although not justified!)

and the effect of electron-induced secondary electron emission from tungsten [44] is included.

Taken together, the data in Fig. 11 show a persistent trend: Φ_{ps} near the separatrix is most positive in LSN discharges, least positive in USN and somewhere between in DN discharges. (However, note that Φ_{ps} obtained by the inner probe are up to ~50 volts different then the other two probes, justifying the level of caution stated here.) The data also suggest that E_r at a location of ρ = ~3 mm becomes progressively more positive in the sequence USN, DN, LSN. Note that a toroidal rotation associated with E_r would correspondingly increase in the co-current direction in the sequence USN, DN, LSN, a behavior that is consistent with the outer probe $V_{//\phi}$ data in Figs. 5 and 7.

3.3.4 Poloidal phase velocity of plasma fluctuations

Previously, the contribution of toroidal plasma rotation to parallel flows near the outer midplane of Alcator C-Mod was studied for normal and reversed field discharges with a fixed, LSN topology [11]. Here, we extend the analysis to the discharges of Figs. 5 and 10, which include LSN, DN, and USN topologies. In this analysis, the $\underline{E}_r \times \underline{B}$ drift velocity of the plasma, $V_{E\times B}$, is estimated from the poloidal phase velocity of plasma fluctuations, V_{ph}. (Some words of caution are also appropriate here. While fluctuation-induced cross-field fluxes inferred by probes may be corrupted by the plasma flux collected by the probe body [45], we are assuming here that the inferred V_{ph} are still characteristic of the unperturbed plasma. In addition, V_{ph} in this context may only be meaningful in regions where the plasma is not broken up into 'blobs' [37, 39], i.e., near the separatrix). Plasma fluctuations are expected to propagate with a superposition of $\underline{E}_r \times \underline{B}$ and drift-wave velocities, V_d,

$$V_{E\times B} = V_{ph} - V_d \quad ; \quad V_d \approx \frac{T_e}{B}\frac{\nabla_r n}{n} + \alpha \frac{\nabla_r T_e}{B} \quad . \qquad (1)$$

The parameter, α, accounts for finite electron temperature fluctuations and is expected to be of

order $\tilde{T}_e n / \tilde{n} T_e$. Fluctuation data [46, 47] suggest this parameter may be near unity in the SOL. Nevertheless, we treat α as an adjustable parameter, $\alpha = 0$ to 1. In Fig. 12, the *poloidal* projections of parallel flow velocity, $V_{//\theta}$, from the outer and vertical probes are plotted versus the corresponding *poloidal* fluid velocities ($\approx V_{E\times B}$), computed from Eq. (1). Good estimates of V_{ph} are obtained at this location (ρ = 4 mm) and a value of α = 1 has been used. The discharges include those of Figs. 5 and 10 but are restricted to those with $|I_p|$ = 0.8 MA and $|B_T|$ = 5.4 tesla.

A clear correlation between the two velocities is exhibited in Fig. 12. For the case of the outer probe, the data fall close to the dashed line that corresponds to a condition of pure toroidal rotation, $V_{\phi\, rot} \sim E_r / B_\theta$, i. e. the poloidal projections of parallel and $\underline{E}_r \times \underline{B}$ flows approximately cancel. Data from the vertical probe do not track the dashed line. For LSN and DN discharges, this might be explained by the presheath effect noted earlier in section 3.2; $V_{//\theta}$ inferred from this probe may be biased towards smaller positive values. However, the USN data (where pre-sheath effects should be absent) also fall below the dashed line. In the USN topology, a net poloidal flow of plasma from the low to high-field side is suggested, in this case driven by $\underline{E}_r \times \underline{B}$ flows.

The above inferences are sensitive to the assumed value of α. As α is reduced, the magnitude of $V_{E\times B}$ computed from Eq. (1) becomes smaller. Consequently, $V_{//\theta}$ becomes uncompensated by the (estimated) $\underline{E}_r \times \underline{B}$ flows and an increasingly larger net poloidal flux is inferred, directed upwards (downwards) in forward (reversed) magnetic field cases. Note that at the outer midplane, the component of $V_{//\theta}$ arising from a Pfirsch-Schlüter ion flow (in a reference frame rotating toroidally, $V_\phi = E_r / B_\theta$) at can be estimated as

$$V_{//\theta}^{PS} \approx -2\varepsilon \frac{\nabla p_i}{nB} \sim -2\varepsilon \frac{\nabla T_e}{B} \,. \qquad (2)$$

For a certain value of α (e.g., $\alpha \sim 1 - 2\varepsilon \sim 0.4$), a re-plot of the outer probe data in Fig. 12 would show $V_{//\theta}$ in excess of pure toroidal rotation (dashed line) and this excess would, by construction,

correspond to a Pfirsch-Schlüter ion flow. Therefore, two principal conclusions follow from these observations: (1) experimental uncertainties prevent us from unfolding separate contributions to $V_{//\phi}$ from toroidal rotation and Pfirsch-Schlüter ion flows, yet, (2) a combination of these two effects can largely account for the observed values of $V_{//\phi}$ in the outer SOL

3.4 Flow observations summary

In summary, data from the inner SOL exhibit clear and consistent results: strong parallel plasma flow directed from low to high-field SOL regions when field lines connect between the two. The principle drive mechanism is patently connected to a strong poloidal asymmetry in the cross-field transport. Data on the outer SOL also exhibit clear trends under magnetic field and x-point reversal; parallel flows are consistent with some combination of toroidal rotation and Pfirsch-Schlüter effects playing a leading role. Using this information as a guide, we now turn toward a flux-tube model to analyze the transport-driven components of the parallel flow and to construct an estimate for the ballooning-like transport asymmetry that drives them.

4. Analysis: transport-driven parallel flows

The data in Fig. 5 were taken from discharges that utilized a nearly mirror-symmetric reflection of flux surface shape in going from LSN to USN. Here we exploit these symmetries to expose the transport-driven component of the parallel flow, i.e., parallel flow arising from cross-field transport and particle balance constraints. As shown in Fig. 8, E_r-driven toroidal rotation and Pfirsch-Schlüter components of parallel flow change sign upon B reversal, while transport-driven parallel flows are expected to retain the same sign. Thus transport-driven flow components can be estimated simply by averaging measurements from forward and reversed B directions. If we assume that divertor geometry does not influence significantly the flows seen outside the divertor region (a reasonable assumption, based on the similarities among the flows here and those seen in JT-60U [10], JET [9] and TCV [12], devices with significantly different divertor geometries), then we can apply the same technique to the set of matched LSN and USN discharges with fixed B

direction (Fig. 5); we need only map the USN data onto the LSN equilibria by mirror-reflecting the flux surfaces and applying a minus sign to the USN flow velocities.

4.1 Flux tube mapping

In a toroidally symmetric system, quantities on a magnetic flux surface can be mapped to the distance along field lines, s, as illustrated in Fig. 13. This 'flux tube coordinate' is normalized to have values running from 0 to 1 as the tube transits from outer to inner divertor legs, starting near the x-point. Velocities directed along increasing s are defined as positive. As an example, the magnetic field strength is plotted versus s, also illustrating a good match between LSN and USN equilibria. An additional benefit of mapping the flow data to this coordinate system is that any systematic offsets in $M_{//}$ (arising from unequal up/down probe areas, for example) will change sign in switching from LSN to USN. Therefore, a simple averaging of data will yield a good estimate of the transport-driven flow component.

Figure 14 shows an example of probe-inferred plasma parameters (at ρ = 4 mm) mapped onto this coordinate system. The data are from the same set of discharges as Fig. 5, binned into three density groupings (color-coded). The symbols represent averaged values while the vertical bars indicate ±1 standard deviation. These flux-tube plots clearly illustrate features noted earlier: lower electron pressures, lower T_e values and near-sonic parallel flows on the inner SOL. As anticipated, the $M_{//}$ data exhibit two components: (1) a persistent trend of parallel plasma flow from outer to inner SOL (the transport-driven component that we are seeking) and (2) systematic offsets about this trend that depend on x-point location (some combination of toroidal rotation, Pfirsch-Schlüter ion flows and Mach-probe offset effects).

The increase of $M_{//}$ with s in Fig. 14 implies that there is a net source of particles into the flux tube, S_{net}; this source must account for the net loss of particles out its ends. In the model described below, we consider the dual constraints of particle and parallel momentum balance in the flux tube. This will allow us to construct a plausible estimate of the magnitude and spatial structure

of S_{net}, given the measured 'input values' of $M_{//}$ (e.g., Fig. 14). Subsequently, we address the poloidal asymmetry in cross-field particle transport that is evidently responsible.

4.2 Flux tube model

Steady-state plasma fluid equations for particle continuity and parallel momentum balance [48] can be written as

$$\nabla \cdot n\underline{v} = S_p, \tag{3}$$

$$m_i n \frac{1}{2} \nabla_{//} v_{//}^2 + \nabla_{//} p \approx m_i n \left[\left(\underline{v}_{//} \cdot \nabla_{//} \right) \underline{v} \right]_{//} + \nabla_{//} p = - m_i n \left[\left(\underline{v}_{\perp} \cdot \nabla_{\perp} \right) \underline{v} \right]_{//} - \left(\nabla \cdot \underline{\underline{\pi}}_i \right)_{//} - \underline{R}_{//ni} - m_i \underline{v}_{//} S_p \tag{4}$$

where S_p is the rate of ionization minus recombination and $\underline{R}_{//ni}$ is the rate of momentum transfer to the neutral species. For simplicity, the electron and ion species are assumed to be sufficiently self-collisional to be Maxwellian with temperatures T_i and T_e. Lacking information on T_i, we further approximate $T_i \approx T_e$. (Note: The isotropization time for ions can be larger than the parallel flow time from the outer to inner midplane, suggesting that a bi-Maxwellian description would be more precise.) The right hand side of Eq. (4) contains parallel momentum source/sink terms. Parallel momentum transfer via turbulence (Reynolds stress, e.g. [49]) could also be included. The most relevant question to address is: Are these terms significant? Data in Fig. 14 suggest that density varies weakly along s. Therefore, the left hand side of Eq. (4) can be approximated as

$$LHS \approx 2\nabla_{//} \left[nT_e \left(1 + \frac{1}{2} M_{//}^2 \right) \right] \quad . \tag{5}$$

The bracketed term is plotted in the bottom panel of Fig. 14. Only a relatively small variation in this quantity is evident (highest density case). Therefore, a good first-approximation is to treat the aggregate of terms on the right hand side of Eq. (4) as being small. (Momentum losses in the divertor regions can in fact be quite high, e.g., plasma detachment, but those regions are excluded here.) While we see that the sum of thermal plus parallel flow energy densities are approximately

constant along the flux tube, a trade-off between them obviously occurs. A simpler and more tractable analytic system that retains this behavior is one where T_e and T_i are approximately constant along field lines. In this case, Eq. (4) (with RHS terms small) becomes

$$\nabla_{//}\left[\ln(n)+\frac{M_{//}^2}{2}\right]\approx 0\ . \tag{6}$$

Note that in order to satisfy Eq. (3), the parallel flux density must be of the form,

$$n\underline{v}_{//}=\underline{B}\,L_{xx}\int\frac{S_p-\nabla\cdot n\underline{v}_{\perp}}{B}\partial s \qquad , \tag{7}$$

where L_{xx} is the length of a field line spanning from s = 0 to 1. Eq. (7) exhibits the following behavior: wherever the net particle source, $S_{net}=S_p-\nabla\cdot n\underline{v}_{\perp}$, is zero along a section of flux-tube, the parallel flux density, if it is nonzero, will vary in proportion to the local magnetic field strength. This response is expected. Similar to the magnetic field, the flux density times the cross-sectional area of the flux-tube must remain constant where S_{net} is zero. Such a 'nozzle effect' can be important. As seen in Fig. 13, the magnetic field strength varies by a factor of two along s. Therefore, a moderate parallel flow at the outer midplane can transform into a near-sonic parallel flow at the inner midplane.

From Eqs. (6) and (7), the parallel Mach number ($M_{//b}$) at location $s=b$ can be related to the Mach number ($M_{//a}$) and density (n_a) at location $s=a$,

$$M_{//b}e^{-\frac{M_{//b}^2}{2}}=e^{-\frac{M_{//a}^2}{2}}B_b\left[\frac{M_{//a}}{B_a}+\frac{L_{xx}}{n_aC_s}\int_a^b\frac{S_{net}}{B}\partial s\right]. \tag{8}$$

A more convenient form is

$$M_{//b}e^{-\frac{M_{//b}^2}{2}}=e^{-\frac{M_{//a}^2}{2}}B_b\left[\frac{M_{//a}}{B_a}+c\int_a^b\frac{f}{B}\partial s\right], \tag{9}$$

with the definitions

$$cf(s) = \frac{S_{net} L_{xx}}{n_a C_s} \quad ; \int_a^b f \partial s = 1 \, . \tag{10}$$

The function, $f(s)$, specifies the shape of S_{net} while the constant, c, specifies its magnitude relative to a characteristic plasma loss rate, $n_a C_s / L_{xx}(b-a)$.

4.3 Flux tube particle source profiles

With the help of Eqs. (9) and (10), we consider the following questions: (1) Can the parallel flow measurements be quantitatively matched for some reasonable net source profile? (2) If so, what is its spatial variation and (3) what is the magnitude of the implied cross-field transport?

The answers to questions (1) and (2) are contained in Fig. 15. Measured values of $M_{//}$ at ρ = 2, 4 and 6 mm (triangles) are shown for matched LSN/USN discharges. Values midway between these (but not greater than $M_{//} = 0.95$) are taken as the 'transport-driven' components of the parallel flow (x symbols). The shape of the net source, $f(s)$, and its magnitude, c, are adjusted until $M_{//}(s)$ from Eq. (9) closely matches the 'data points'. Resultant S_{net} profiles are shown as dashed curves in Fig. 15. While the solutions are not unique, they clearly demonstrate that a quantitative match to plasma flow measurements can be obtained. The solutions also show the type of poloidal asymmetry that is required of the S_{net}, which is expected to be closely related to the spatial variation of cross-field transport fluxes. (However, these quantities are not necessarily proportional; see below.)

4.4 Plasma circulation and cross-field transport asymmetries

Note that a steady-state plasma flow loop is implied by the results shown in Fig. 15: excess plasma enters flux tubes near the outer SOL; a large fraction of this flows along field lines to the inner SOL and presumably neutralizes at or near the inner divertor surface (via surface or volume recombination). In order to close the loop, neutrals likely ionize inside the separatrix near the inner divertor leg; the resulting ions are free to over-populate flux tubes in the outer SOL once again.

(Another possible but unlikely scenario is the convection of plasma, rather than neutrals, inside the separatrix near the inner divertor.) It is important to note that neutral ionization in the outer SOL, S_p, is not part of this flow loop. Although a large ionization source is indeed found in the outer SOL of Alcator C-Mod, it is primarily associated with a different flow loop: one of cross-field transport onto main-chamber wall surfaces and associated recycling [50].

In light of these considerations, the net particle source can be approximated as

$$S_{net} = S_p - \nabla \cdot n\underline{v}_\perp \approx \left(S_p - \frac{\partial n v_r^{mc}}{\partial r} \right) - \frac{\partial n v_r^{so}}{\partial r} \approx - \frac{\partial n v_r^{so}}{\partial r} \ , \qquad (11)$$

where S_p is balanced primarily by the radially increasing plasma fluxes associated with main-chamber recycling, nv_r^{mc}. The flux, nv_r^{so}, is the only component that is truly 'scraped-off'; this flux yields an excess of particles that must be 'drained' by parallel flows to the divertors. The spatial profiles of S_{net} shown in Fig. 15 can therefore be viewed as representing the quantity, nv_r^{so} / λ_n, where λ_n is a characteristic density gradient scale length. However, since nv_r^{so} is only part of the total cross-field flux, the spatial variation in S_{net} does not necessarily indicate the spatial variation in total cross-field transport, nv_r^{total}; the main-chamber recycling flux must also be included.

In the low-density discharges of Fig. 15, S_{net} exhibits a classic ballooning structure – peaked near the outer midplane. In these discharges, the ratio of main-chamber to divertor recycling is the lowest. Therefore, the spatial variation of S_{net} may be indicative of the underlying poloidal asymmetries in the cross-field transport fluxes, $nv_r^{so} \propto nv_r^{total}$. However, as plasma density is raised, the peak in S_{net} offsets in a direction toward the inner divertor. Although one can not rule out the possibility that the poloidal asymmetry of the underlying transport has correspondingly changed, the shift in S_{net} is more likely related to the increase in main-chamber recycling that is

observed at higher densities [50]. The same ballooning-like poloidal structure may still be present; it could be just that a larger fraction of the total cross-field flux near the outer midplane tends to exhaust onto main-chamber wall surfaces.

4.5 Magnitude of cross-field transport

Our final task is to characterize the magnitude of nv_r^{so} and to relate it to results from previous transport analyses. A flux-tube averaged value of nv_r^{so} can be expressed in terms of effective convection (V_{eff}) and diffusion (D_{eff}) coefficients,

$$\frac{n_a V_{eff}}{\lambda_n} \equiv \left\langle -\frac{\partial n v_r^{so}}{\partial r} \right\rangle \approx \frac{1}{b-a}\int_a^b S_{net}\,\partial s = \frac{c}{b-a}\frac{n_a C_s}{L_x} \quad , \qquad (12)$$

$$D_{eff} \equiv V_{eff}\lambda_n \, ,$$

where n_a and λ_n are the density and its e-folding length near the outer midplane. The interval $[a,b]$ corresponds to the flux tube segment between probe measurements.

A compilation of V_{eff} and D_{eff} values is shown in Table 1. The magnitudes are comparable to those obtained from earlier UEDGE modeling [51] and from SOL particle balance measurements [39, 50, 52] in similar discharges. These previous studies identified a systematic increase of cross-field transport with distance from the separatrix and with discharge density, a trend reproduced in Table 1. Although the earlier studies were based on poloidally uniform transport coefficients – a situation clearly contrary to the new information here – the principal conclusions appear to remain valid. We anticipate that the main effects of properly accounting for poloidal transport asymmetries in SOL models would be: (1) reproduction of observed plasma flow patterns, including the strong flows in high-field SOL, (2) more accurate inference of cross-field transport coefficients, and (3) determination of the topology-dependent flow boundary conditions imposed by the SOL on the confined plasma.

5. Topology-dependent flow boundary conditions and plasma rotation

As a result of transport-driven parallel flows, the SOL plasma can develop a net volume-averaged toroidal momentum (illustrated in Fig. 16a): co-current directed for $B \times \nabla B$ pointing toward the x-point and counter-current directed otherwise. An important question is: do these SOL flows affect the plasma inside the separatrix? Intuitively, we expect the confined plasma to react to these different flow boundary conditions with a change in its toroidal rotation – a reaction that incurs minimal resistance in this axisymmetric geometry. However, the magnitude of such a response would ultimately depend on the details of the momentum transfer mechanisms, in particular, their poloidal variation and sensitivity to the strong SOL flows that occur in the high-field region.

Exploring these ideas, toroidal velocities measured near the separatrix from the three Mach probes ($V_{//\phi}$) and in the plasma center from Ar^{17+} ions are assembled in Fig. 17. The data are binned and plotted versus $\overline{n}_e$. Discharge conditions were $I_p = 0.8$ MA, $B_T = 5.4$ tesla, and $B \times \nabla B$ pointing down. A remarkable correlation is revealed among the flow measurements: a co-current velocity increase of ~15 km s^{-1}, detected by the outer and vertical probes in going from USN to LSN, is systematically matched by a comparable change in core plasma rotation. These topology-dependent increments in toroidal velocity also exhibit a similar sensitivity to $\overline{n}_e$, becoming diminished at low densities. In contrast, toroidal velocities detected at the inner probe location behave somewhat differently: they exhibit a factor of ~3 larger step change toward the co-current direction in going from USN to LSN and display no sensitivity to $\overline{n}_e$.

These data demonstrate that topology-dependent SOL flows can indeed influence the confined plasma. The near-sonic flow on the inner SOL appears to be the source of the overall rotation-drive; it is the largest velocity in the system and its change with topology is insensitive to discharge parameters. Apparently, the net coupling of this flow momentum into the confined plasma can vary with discharge conditions (e.g. $\overline{n}_e$).

In other discharges (I_p = 0.8 MA, B_T = 5.4 tesla, $\overline{n}_e$ =1.5x10^{20} m^{-3}), we have explored the sensitivity of SOL flows and core plasma rotation to magnetic flux balance, parameterized here as the distance between primary and secondary separatrix mapped to the outer midplane (Fig. 18). These data verify a close coupling between SOL flows and core rotation: the central and edge velocities (outer probe) are seen to have a proportionality of roughly ~1.5 in Fig. 18b. The velocities also display a remarkable sensitivity to magnetic topology: a ~5 mm shift in the x-point balance is sufficient to completely reverse the flows. This size scale is comparable to the pressure gradient scale lengths near the separatrix (Fig. 5) – an expected result if in/out pressure asymmetries on open field lines are the principle drive mechanism.

Another interesting and testable consequence of the transport-driven toroidal rotation hypothesis is its feedback (via momentum transfer) on the SOL; the helical flow pattern should be partially converted into a toroidal rotation that mimics the confined plasma's response. Also, since the radial electric field is intimately connected to toroidal rotation, a correspondingly more positive (less positive) E_r should be seen in the SOL for $B \times \nabla B$ pointing toward (away from) the x-point (see Fig. 16b). As discussed earlier, the data in Figs. 5 and 11 show precisely these tendencies: stronger co-current rotation and more positive E_r in LSN, weaker co-current rotation and less positive E_r in USN.

The latter observations are particularly intriguing. Radial electric field gradients and associated $\underline{E} \times \underline{B}$ velocity shear have been identified [53-55] to regulate cross-field transport: the L-H confinement mode transition is thought involve a bifurcation in plasma transport characteristics near the vicinity of the separatrix [56], triggered by the attainment of a certain level of velocity shear [57]. In addition, magnetic topology is well known to affect the L-H threshold [58]; generally, higher powers are required when $B \times \nabla B$ points away from rather than toward the active x-point. Yet, no compelling explanation for this behavior has advanced. The experimental results reported

here point to a possible explanation: transport-driven SOL flows, modulated by magnetic topology, affect radial electric fields, and by inference, flow shear near the separatrix.

6. SOL flows, core plasma rotation and L-H threshold

We have recently investigated the effect of magnetic topology (LSN, DN, USN) on the L-H power threshold in Alcator C-Mod, with specific emphasis on SOL flows and toroidal rotation of the confined plasma. Strong circumstantial evidence has been found that supports the hypothesis advanced above, namely, transport-driven SOL flows set topology-dependent boundary conditions that influence the L-H transition.

The time-evolutions of three discharges that exhibited an L-H transition are shown in Fig. 19. Prior to application of ICRF power, these ohmic L-mode target plasmas had similar external control parameters (I_p=0.8 MA, B_T=5.4 tesla, $\overline{n}_e$ = 1.4x10^{20} m^{-3}, $B \times \nabla B$ down) but different magnetic topologies (USN, DN, LSN). Electron temperatures measured by ECE and edge Thomson scattering [59] as well as electron pressure gradients near the 95% magnetic flux surface are nearly identical in the ohmic L-mode phases. A similar observation has been noted on DIII-D; edge profiles remained unchanged in switching from LSN to USN [60]. However, important differences are revealed here in the core rotation during the ohmic phase, stepping from ~ -50, -30, 0 km s^{-1} in the sequence USN, DN, LSN. As discussed above and shown in Figs. 17 and 18, this behavior can be understood in terms of the boundary conditions imposed by SOL flows. Therefore, despite superficial similarities, the target plasma conditions are in fact fundamentally different, e.g. topology-dependent toroidal rotation and associated electric fields near the separatrix.

ICRF heating power is applied at levels close to the L-H threshold (0.9, 1.6, 2.9 MW) to yield a transition later in time. This power is from 2 two-strap antennas (80 MHz, 0 - π phasing) and one four-strap antenna (78 MHz, 0 - π - 0 - π phasing) using a hydrogen minority heating scenario. It is important to note that this heating method imparts no momentum input to the plasma. In response to the RF power, edge electron temperatures and pressure gradients evolve, most

notably for high input powers (USN). At the time of L-H transition, the edge electron temperature is approximately a factor of 2 higher in the USN case; pressure gradients are correspondingly higher. These results are consistent with earlier findings for discharges with forward versus reversed magnetic field and fixed x-point location [61, 62] and point to a puzzle not explained satisfactorily by present theoretical models: threshold studies consistently show a transition condition related to edge electron temperature, but it is topology dependent. The central toroidal velocity is also seen to ramp toward the co-current direction in response to increased auxiliary power (discussed further below). Remarkably, at the time of L-H transition, the velocity achieves a level near ~ 0 km s^{-1}, independent of magnetic topology!

A comparison of toroidal velocities measured at the plasma center and 2 mm outside the separatrix is shown in Fig. 20. These discharges are similar to those of Fig. 19 but had different ICRF power levels. Unfortunately, owing to the high power densities, the probes were restricted to $\rho \geq 2$ mm and could not be operated at all in the highest power discharges. Nevertheless, the correspondence between central and near-separatrix velocities in these ICRF-heated L-mode phases is similar to that in ohmic L-mode plasmas (such as in Fig. 18b, with a proportionality of roughly ~1.5). Apparently, the central velocity simply follows changes in plasma rotation near the separatrix (perhaps with a time-delay, as seen during the L-H transition [23]). In effect, central rotation is a crude measure of the separatrix plasma rotation during the L-mode phase and, by inference, relates to the radial electric field there (allowing for offsets that may include rotation profile effects).

These data suggest that at least two elements can control plasma rotation near the separatrix, both of which appear to influence L-H transition physics in a somewhat additive fashion for these discharges: SOL flow boundary conditions, which change in going from LSN to USN, and a co-current flow drive mechanism, perhaps related to the edge plasma pressure gradients that are affected by input power. We do not offer an explanation for the latter response here. However, a similar effect has been observed during the H-mode phase of ohmic or ICRF heated plasmas [25]; the level of central plasma rotation was found to correlate with plasma stored energy. A number of

explanations have been advanced for this behavior, including theories based on plasma turbulence [63, 64] and sub-neoclassical transport [65].

Finally, it is important to note that during the H-mode phase, the correspondence between probe-inferred separatrix plasma rotation and central plasma rotation is lost; the central plasma can co-rotate at speeds up to 120 km s^{-1}. These observations indicate that the toroidal rotation profile inside the separatrix changes dramatically during H-mode. Thus, while SOL flow boundary conditions appear to affect the L-H transition, they do not appear to play a dominant role in setting the rotation of the core plasma once the H-mode is achieved.

7. Summary and Conclusions

Detailed measurements of plasma profiles, including flows, in the low-field (inner) and high-field (outer) side scrape-off layer regions of Alcator C-Mod have been performed in discharges with different magnetic separatrix topologies (upper-, lower-, and double-null) and with a range of plasma densities. By a variety of measures, these data reveal a strong poloidal asymmetry (ballooning-like) in cross-field transport: T_e gradients along field lines, in/out variation in fluctuation levels (persistent in single-null) and in/out pressure asymmetries (particularly evident in double-null). Dramatic, near-sonic parallel plasma flows are detected in the high-field SOL. These flows tend to reverse sign in changing from upper to lower x-point location and are robustly insensitive to discharge density for the factor of ~2 variation studied. The drive mechanism is clearly connected to a ballooning-like transport asymmetry, hence their designation as *transport-driven flows*. In contrast, parallel flows on the outer SOL are not as strong (factor of ~3 smaller), modulate with x-point changes, but tend to remain in the co-current direction. They also exhibit a clear sensitivity to discharge density. This behavior, plus separate information on poloidal velocities, suggests that these flows are more closely associated with toroidal plasma rotation and Pfirsch-Schlüter ion currents.

A simple magnetic flux-tube model is used to explore the transport-driven component of the

flows. Measurements indicate that thermal plus flow energy density is roughly constant along a flux-tube. However, the reduction in flux-tube cross-section in the high-field region can lead to a 'nozzle effect', accelerating the local plasma flow. A match between measured and modeled flow velocities can be achieved by postulating a very strong ballooning-like asymmetry to the cross-field transport. The implied cross-field convection and diffusion coefficients are found similar in magnitude to those from previous analyses, including the trends of increasing transport with distance from the separatrix and discharge density. The model also clearly demonstrates that transport-driven flows can lead to a net volume-averaged toroidal momentum in the SOL, co-current directed when $B \times \nabla B$ is pointing towards the x-point, counter-current directed otherwise.

With regard to impurity transport in the SOL, the overall plasma convection pattern would appear to promote the migration of impurities born from main-chamber plasma-wall contact toward the inner divertor strike point (particularly from high-field side wall surfaces, as demonstrated directly from impurity 'plume' dispersal experiments). However, the flow pattern does not appear to allow impurities to be swept directly from the outer to inner divertor; the net poloidal flow is found to be stagnant near the outer midplane. Such a flow field is broadly consistent with one that has been speculated to exist in JET to explain the buildup of carbon in the inner divertor [66] and to account for plasma flow observations at the top of the vessel [9]. The flow field is also consistent with recent measurements of ^{13}C deposition following $^{13}CH_4$ injection in JET [67]: $^{13}CH_4$ injected at the top of the vessel resulted in ^{13}C deposition on the inner divertor tiles.

A comparison of toroidal plasma flow velocities measured near the separatrix (via probes) with that in the plasma center (via Ar^{17+} Doppler) shows the two to be closely connected; in changing from upper to lower-null with $B \times \nabla B$ pointing down, both exhibit an incremental change toward the co-current direction. The change in central plasma rotation is found to be nearly proportional to that measured at the separatrix in the low-field side SOL. These data clearly demonstrate that SOL flows can impose influential boundary conditions on the confined plasma. Moreover, transport-driven flows appear to affect toroidal rotation in the SOL itself; a stronger

(weaker) radial electric field is evident when $B \times \nabla B$ is pointing toward (away from) the x-point. These observations are particularly intriguing since they suggest a broader connection to L-H threshold physics: radial electric field gradients (velocity shear) at the edge are thought to play a key role while magnetic topology is known empirically to affect L-H power thresholds.

Results from a set of matched ICRF-heated discharges are presented, exploring the behavior of central plasma rotation and SOL flows as the L-H transition is approached in upper-, lower- and double-null topologies. Remarkably, the L-H transition is found to be coincident with central rotation achieving roughly the same value in these discharges, independent of topology. Since transport-driven SOL flows tend to impede co-current rotation in upper-null, a higher input power (which tends to spin the plasma in the co-current direction) is correspondingly required. We recognize that the physics controlling the L-H transition is expected to involve plasma flow gradients (i.e., $\underline{E} \times \underline{B}$ shear zones) that are not directly measured in these experiments. Nevertheless, these results clearly link the boundary conditions imposed by SOL flows to the empirically observed topology-dependence of the L-H power threshold.

Acknowledgements

We thank Ben Carreras for his constructive comments on this manuscript. The data presented in this paper would not have been collected without the continuing dedication and hard work of the engineers, technical staff, students and scientists on the Alcator team. This work is supported by U.S. D.o.E. Coop. Agreement DE-FC02-99ER54512.

References

[1] Wan, A.S., LaBombard, B., Lipschultz, B., and Yang, T.F., J. Nucl. Mater. **145-147** (1987) 191.
[2] Vershkov, V.A., Grashin, S.A., and Chankin, A.V., J. Nucl. Mater. **145** (1987) 611.
[3] Vershkov, V.A., J. Nucl. Mater. **162** (1989) 195.
[4] Pitts, R.A., Vayakis, G., Matthews, G.F., and Vershkov, V.A., J. Nucl. Mater. **176** (1990) 893.
[5] Boucher, C., MacLatchy, C.S., Le Clair, G., Lachambre, J.L., and St-Onge, M., J. Nucl. Mater. **176** (1990) 1050.
[6] MacLatchy, C.S., et al., J. Nucl. Mater. **196-198** (1992) 248.
[7] LaBombard, B., et al., J. Nucl. Mater. **241-243** (1997) 149.
[8] Asakura, N., et al., Nucl. Fusion **39** (1999) 1983.
[9] Erents, S.K., Chankin, A.V., Matthews, G.F., and Stangeby, P.C., Plasma Phys. Control. Fusion **42** (2000) 905.
[10] Asakura, N., et al., J. Nucl. Mater. **313-316** (2003) 820.
[11] LaBombard, B., Gangadhara, S., Lipschultz, B., and Pitcher, C.S., J. Nucl. Mater. **313-316** (2003) 995.
[12] Horacek, J., Pitts, R.A., and Wischmeier, M., submitted to J. Nucl. Mater. (2004).
[13] Philipps, V., Roth, J., and Loarte, A., Plasma Phys. Control. Fusion **45** (2003) 17.
[14] Hugill, J., J. Nucl. Mater. **196** (1992) 918.
[15] Chankin, A.V., et al., J. Nucl. Mater. **290** (2001) 518.
[16] Chankin, A.V. and Stangeby, P.C., Nucl. Fusion **41** (2001) 421.
[17] Porter, G.D., et al., J. Nucl. Mater. **313-316** (2003) 1085.
[18] Rozhansky, V., et al., J. Nucl. Mater. **313-316** (2003) 1141.
[19] Asakura, N., et al., Phys. Rev. Lett. **84** (2000) 3093.
[20] Asakura, N., et al., in Fusion Energy 2002 (Proc. 19th Int. Conf. Lyon, 2002), IAEA, Vienna (2003), CD ROM file EXD1_3 and http://www.iaea.org/programmes/ripc/physics/fec2002/html/fec2002.htm.
[21] LaBombard, B. and Lipschultz, B., Nucl. Fusion **27** (1987) 81.
[22] Rozhansky, V. and Tendler, M., Phys. Plasmas **1** (1994) 2711.
[23] Rice, J.E., et al., Nucl. Fusion **44** (2004) 379.
[24] Lee, W.D., et al., Phys. Rev. Lett. **91** (2003) 205003.
[25] Rice, J.E., et al., Nucl. Fusion **41** (2001) 277.
[26] Smick, N., LaBombard, B., and Pitcher, C.S., submitted to J. Nucl. Mater. (2004).
[27] Hutchinson, I.H., et al., Phys. Plasmas **1** (1994) 1511.
[28] Hutchinson, I.H., Phys. Rev. A **37** (1988) 4358.
[29] LaBombard, B., et al., J. Nucl. Mater. **266-269** (1999) 571.
[30] Pitcher, C.S., et al., Rev. Sci. Instrum. **72** (2001) 103.
[31] Matthews, G.F., et al., Plasma Phys. Control. Fusion **32** (1990) 1301.
[32] Granetz, R.S., Hutchinson, I.H., Gerolamo, J., Pina, W., and Tsui, C., Rev. Sci. Instrum. **61** (1990) 2967.
[33] Lao, L.L., et al., Nucl. Fusion **25** (1985) 1611.
[34] Rice, J.E., et al., Nucl. Fusion **38** (1998) 75.
[35] Hutchinson, I.H., Rice, J.E., Granetz, R.S., and Snipes, J.A., Phys. Rev. Lett. **84** (2000) 3330.
[36] Hutchinson, I.H., *Principles of plasma diagnostics* (Cambridge University Press, Cambridge; New York, 2002).
[37] Terry, J.L., et al., Phys. Plasmas **10** (2003) 1739.
[38] Boswell, C.J., Terry, J.L., LaBombard, B., Lipschultz, B., and Pitcher, C.S., submitted to Plasma Phys. Control. Fusion (2004).
[39] LaBombard, B., et al., Phys. Plasmas **8** (2001) 2107.

[40] Gangadhara, S. and LaBombard, B., submitted to Plasma Phys. Control. Fusion (2004).
[41] Jablonski, D., et al., J. Nucl. Mater. **241-243** (1997) 782.
[42] Greenwald, M., et al., Nucl. Fusion **28** (1988) 2199.
[43] Stangeby, P.C., Phys. Fluids **27** (1984) 682.
[44] Langley, R.A., et al., *Data compendium for plasma-surface interactions*, Nuclear Fusion, Special Issue, IAEA, Vienna (1984).
[45] LaBombard, B., Phys. Plasmas **9** (2002) 1300.
[46] Meier, M.A., Bengtson, R.D., Hallock, G.A., and Wootton, A.J., Phys. Rev. Lett. **87** (2001) 085003/1.
[47] Boedo, J.A., et al., Phys. Plasmas **8** (2001) 4826.
[48] Braginskii, S.I., in Reviews of Plasma Physics (1965), Consultants Bureau, New York Vol. 1, 205.
[49] Hidalgo, C., et al., Phys. Rev. Lett. **91** (2003) 065001.
[50] LaBombard, B., et al., Nucl. Fusion **40** (2000) 2041.
[51] Umansky, M.V., Krasheninnikov, S.I., LaBombard, B., Lipschultz, B., and Terry, J.L., Phys. Plasmas **6** (1999) 2791.
[52] Labombard, B., et al., in Fusion Energy 2002 (Proc. 19th Int. Conf. Lyon, 2002), IAEA, Vienna (2003), CD ROM file EXD2_1 and http://www.iaea.org/programmes/ripc/physics/fec2002/html/fec2002.htm.
[53] Biglari, H., Diamond, P.H., and Terry, P.W., Phys. Fluids **2** (1990) 1.
[54] Burrell, K.H., Phys. Plasmas **4** (1997) 1499.
[55] Terry, P.W., Rev. Mod. Phys. **72** (2000) 109.
[56] Connor, J.W. and Wilson, H.R., Plasma Phys. Control. Fusion **42** (2000) 1.
[57] Groebner, R.J., Burrell, K.H., and Seraydarian, R.P., Phys. Rev. Lett. **64** (1990) 3015.
[58] Ryter, F. and H Mode Database Working Group, Nucl. Fusion **36** (1996) 1217.
[59] Hughes, J.W., et al., Rev. Sci. Instrum. **72** (2001) 1107.
[60] Carlstrom, T.N., et al., Nucl. Fusion **39** (1999) 1941.
[61] Hubbard, A.E., et al., in Plasma Physics and Controlled Fusion Research (Proc. 16th Int. Conf. Montreal, 1996), IAEA, Vienna (1997) Vol. 1, 875.
[62] Hubbard, A.E., et al., Plasma Phys. Control. Fusion **40** (1998) 689.
[63] Shaing, K.C., Phys. Rev. Lett. **86** (2001) 640.
[64] Coppi, B., Nucl. Fusion **42** (2002) 1.
[65] Rogister, A.L., Rice, J.E., Nicolai, A., Ince-Cushman, A., and Gangadhara, S., Nucl. Fusion **42** (2002) 1144.
[66] Coad, J.P., et al., J. Nucl. Mater. **290-293** (2001) 224.
[67] Likonen, J., et al., Fusion Engineering and Design **66-68** (2003) 219.

Table 1. Flux-tube averaged cross-field transport coefficients corresponding to the net particle source profiles in Fig. 15.

$\overline{n}_e$ (10^{20} m^{-3})	ρ (mm)	c	V_{eff} (m s^{-1})	D_{eff} (m^2 s^{-1})
1.0	2	0.20	7.7	0.06
	4	0.36	14	0.15
	6	0.42	19	0.32
1.5	2	0.16	7.2	0.07
	4	0.34	15	0.19
	6	0.41	16	0.23
2.0	2	0.29	18	0.27
	4	0.42	28	0.56
	6	0.45	32	0.84

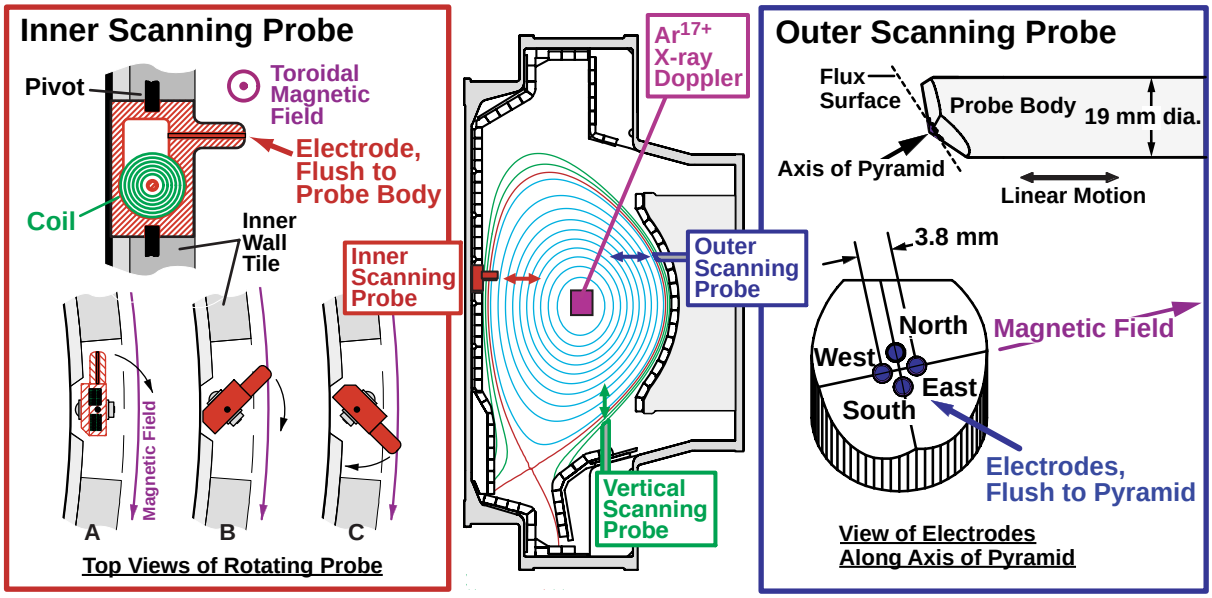

Figure 1. Scanning Langmuir-Mach probes are used to infer simultaneously plasma profiles and parallel flows at three locations in the scrape-off layer of Alcator C-Mod, including the high-field side (Inner Scanning Probe). In addition, core plasma rotation is inferred from the Doppler-shifts of central Ar^{17+} ions. A typical lower single-null (LSN) plasma equilibrium is shown.

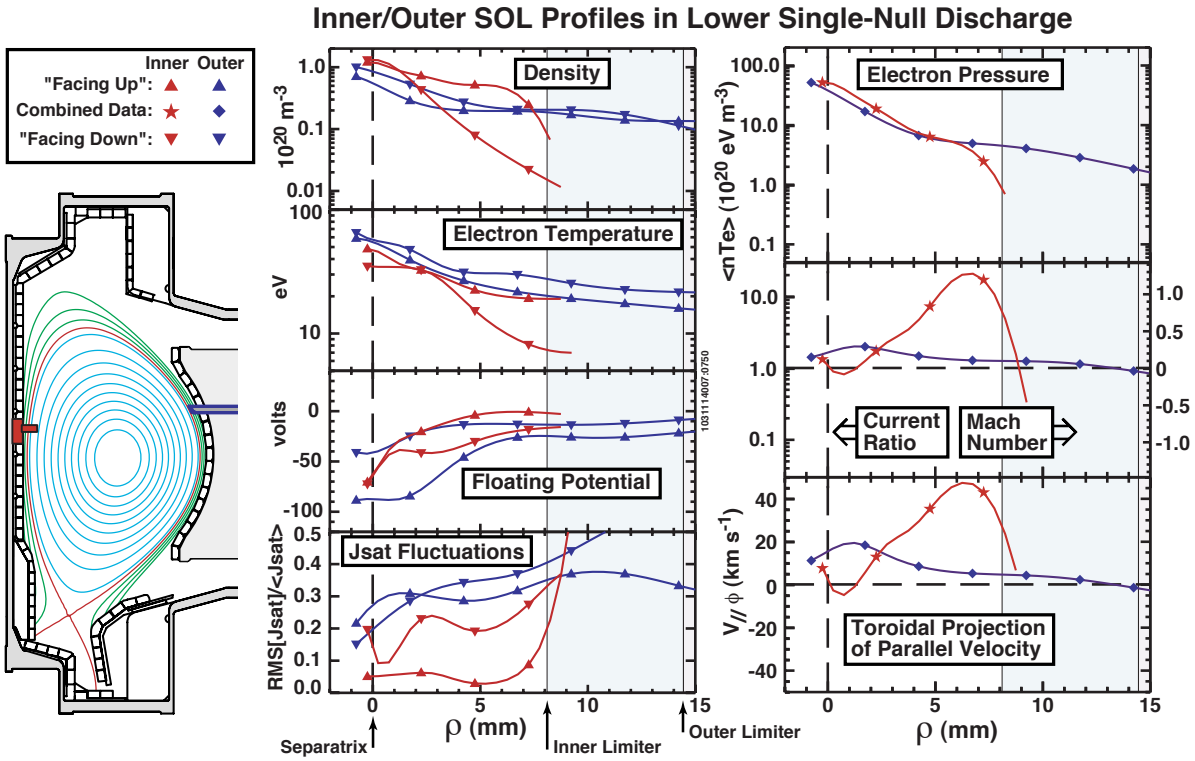

Figure 2. Magnetic equilibrium for lower single-null discharge and corresponding profile data recorded in the inner and outer regions of the scrape-off layer.

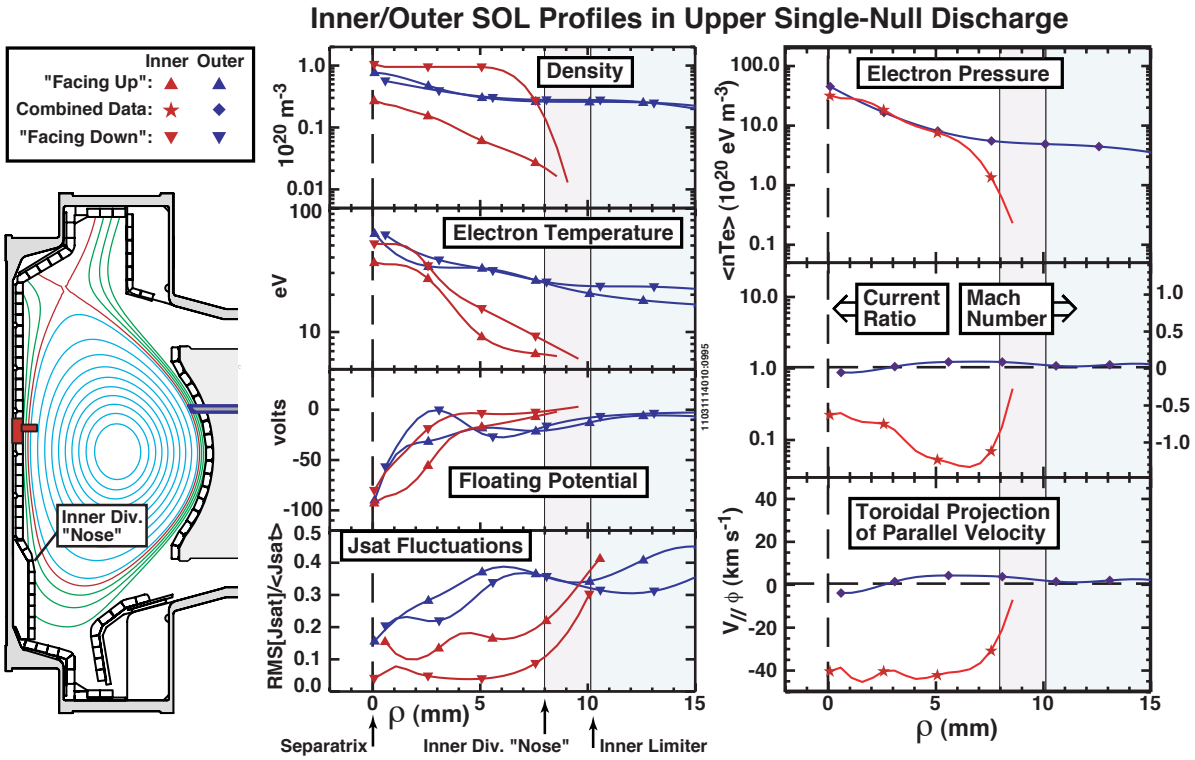

Figure 3. Same as Fig. 2 for upper single-null discharge.

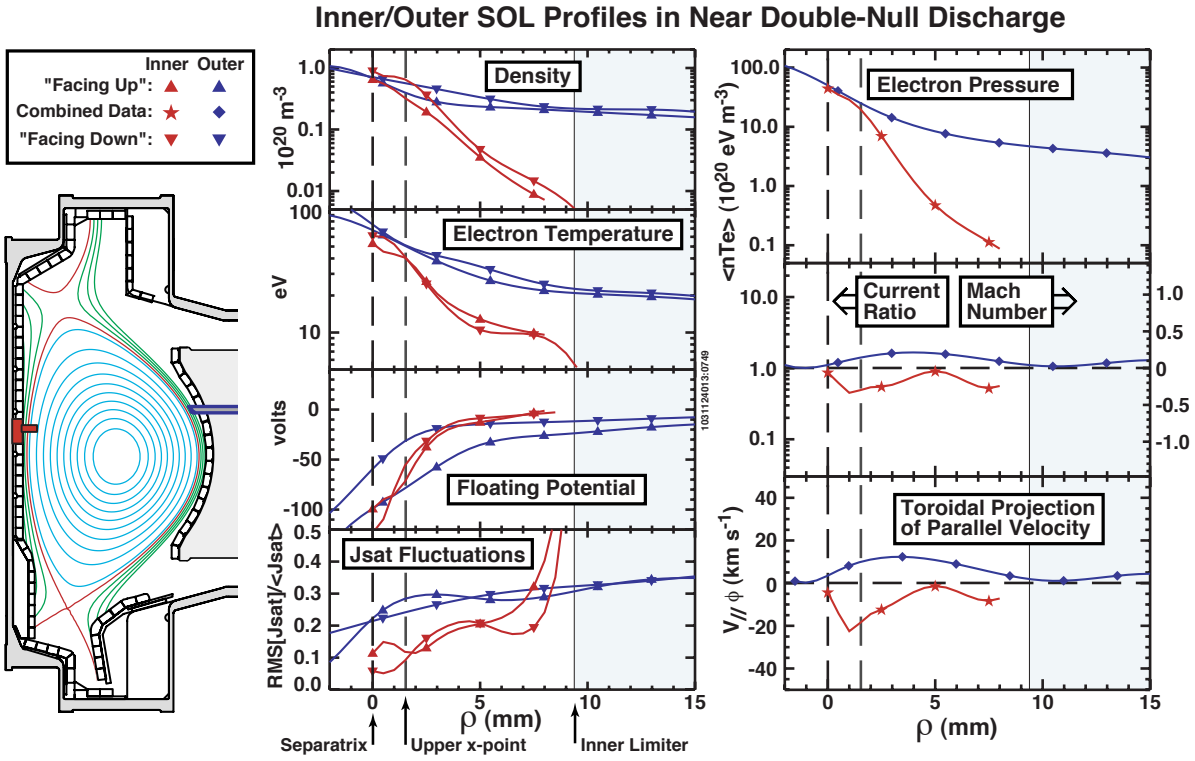

Figure 4. Same as Fig. 2 for near double-null discharge.

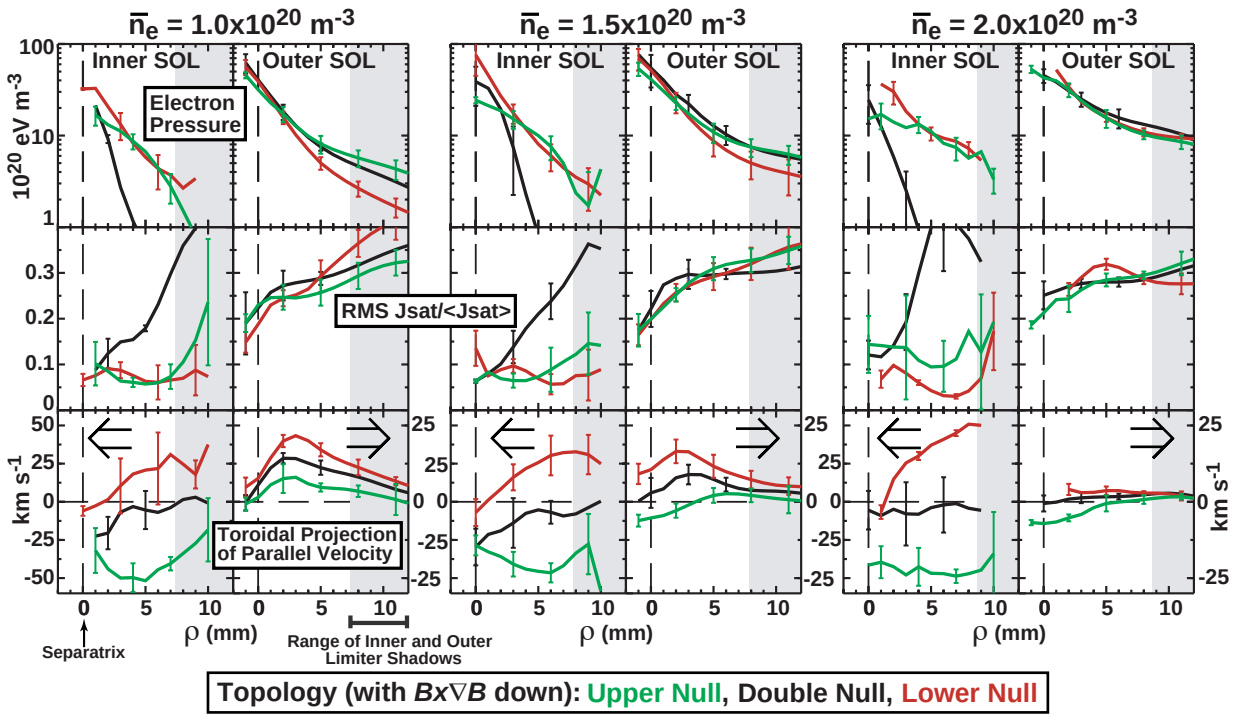

Figure 5. A compilation of inner and outer SOL profiles from 112 probe scans. Line-averaged density and magnetic topology were varied with otherwise identical conditions.

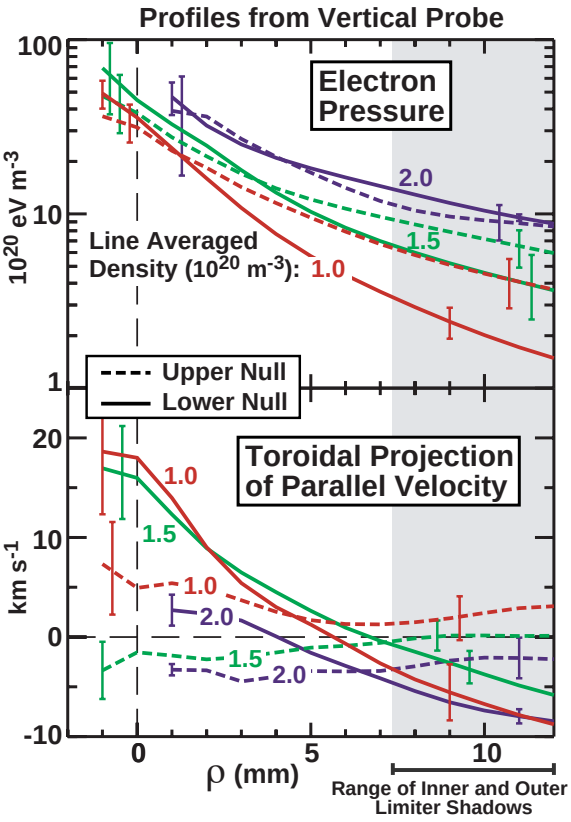

Figure 6. Profiles at the vertical probe location corresponding to the data shown in Fig. 5.

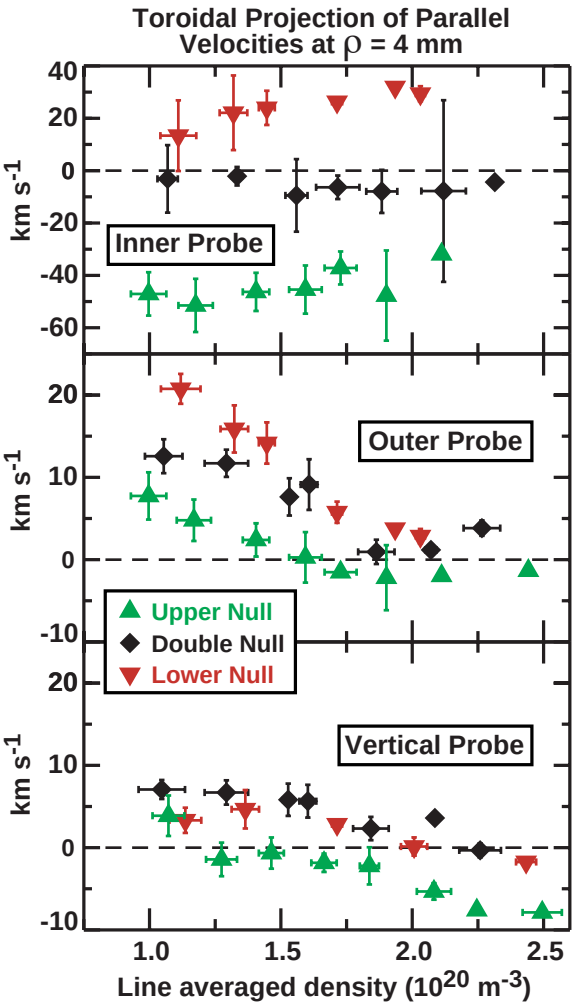

Figure 7. Toroidal projection of parallel flows versus $\overline{n}_e$ for the data set of Fig. 5. Data are binned in $\overline{n}_e$ increments. Bars indicate ±1 standard deviation, computed from sample variance.

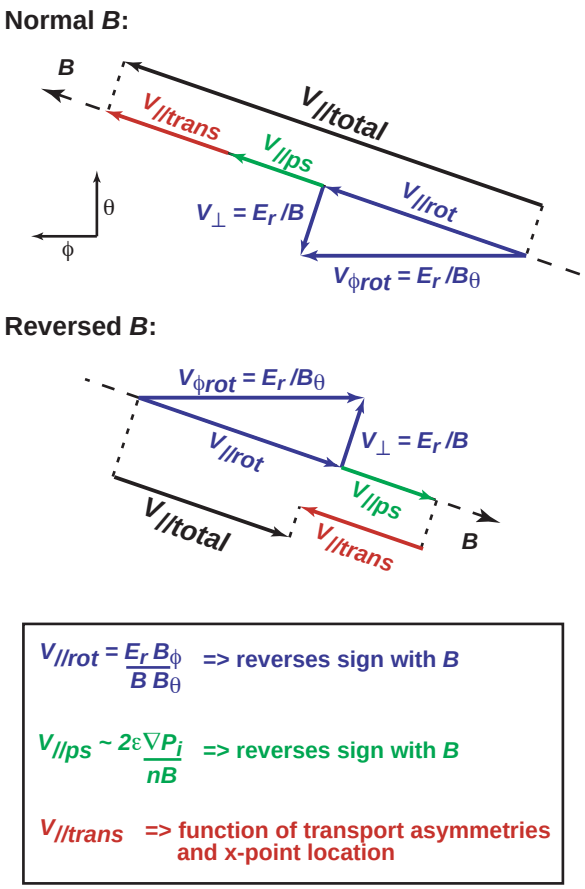

Figure 8. Magnetic fields and representative plasma flow components at the outer midplane, as viewed inward along a major radius. Mach probes measure the total parallel flow ($V_{//\,total}$). Parallel flow components arising from Pfirsch-Schlüter ion currents ($V_{//\,ps}$) and toroidal rotation ($V_{//\,rot}$) reverse when B_T and I_p are reversed. In contrast, parallel flow components driven by cross-field transport ($V_{//\,trans}$) are expected to be insensitive to field direction but possibly dependent on x-point location (particularly in the high-field SOL), if cross-field transport exhibits a strong ballooning-like character. Other flows, such as those arising from ionization imbalances, are omitted for clarity.

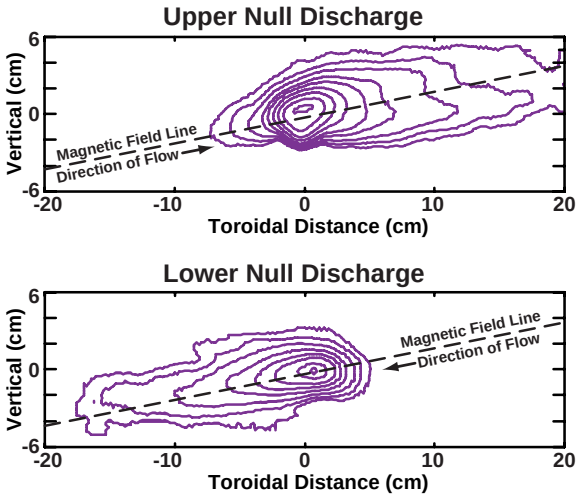

Figure 9. Contour plots of C^{+1} dispersal (515 nm light, viewed along major radius direction) resulting from CH_4 injection at the inner wall, midplane location [41]. These data show strong plasma flow directed primarily along field lines in the inner SOL, with a clear dependence on LSN/USN topology.

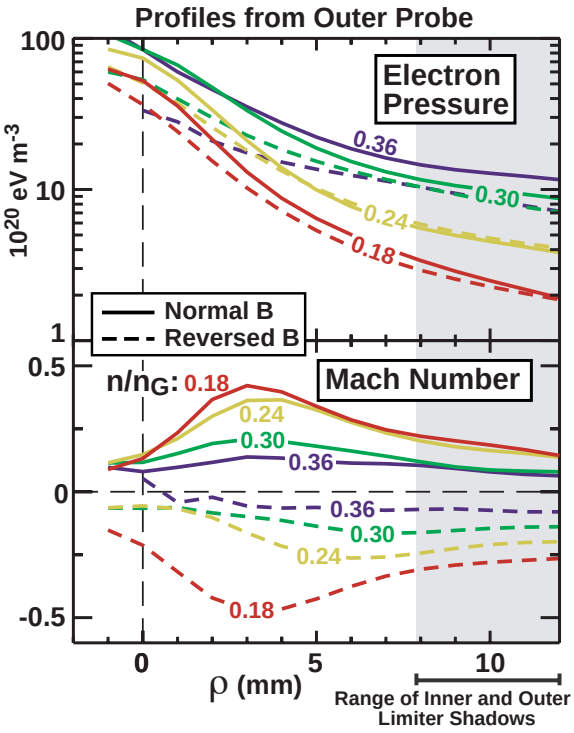

Figure 10. Comparison of outer probe electron pressure and Mach number profiles for forward and reversed magnetic field (I_p and B_T aligned). The parallel Mach flow is found to remain in the direction of I_p (positive for normal *B*, negative for reversed *B*).

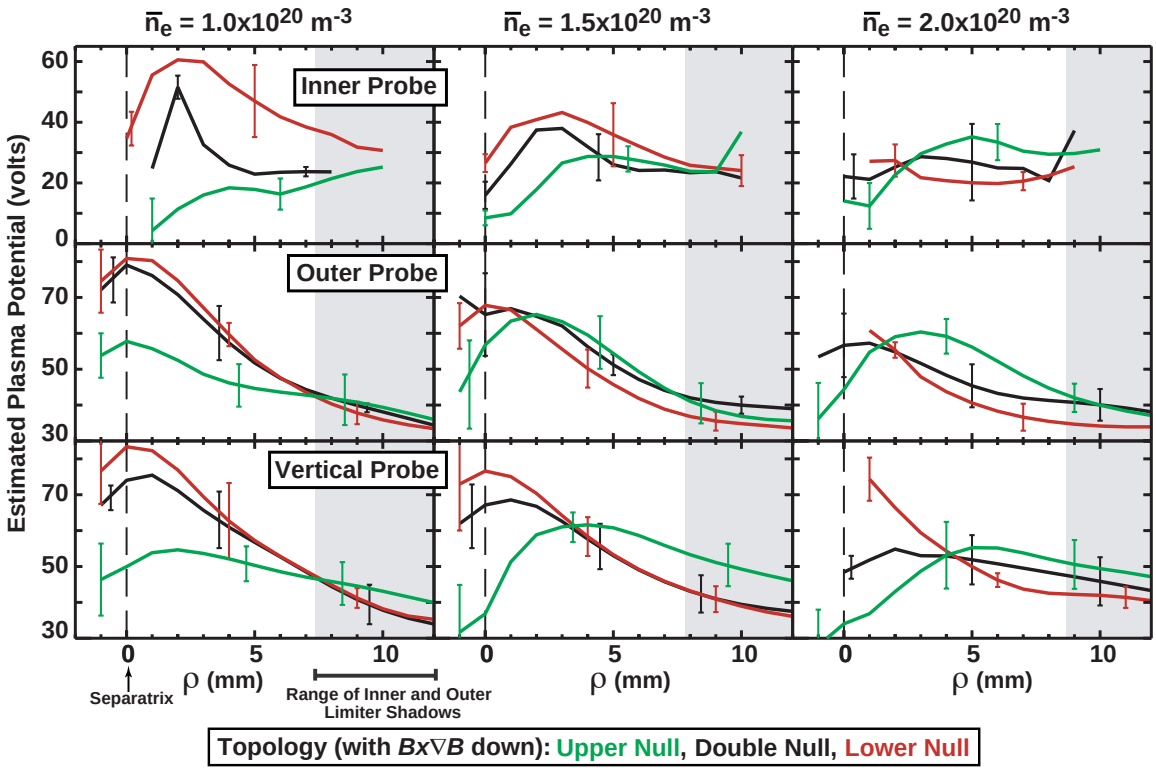

Figure 11. Probe-sheath estimated plasma potential profiles. Data are for the same set of discharges represented in Fig. 5.

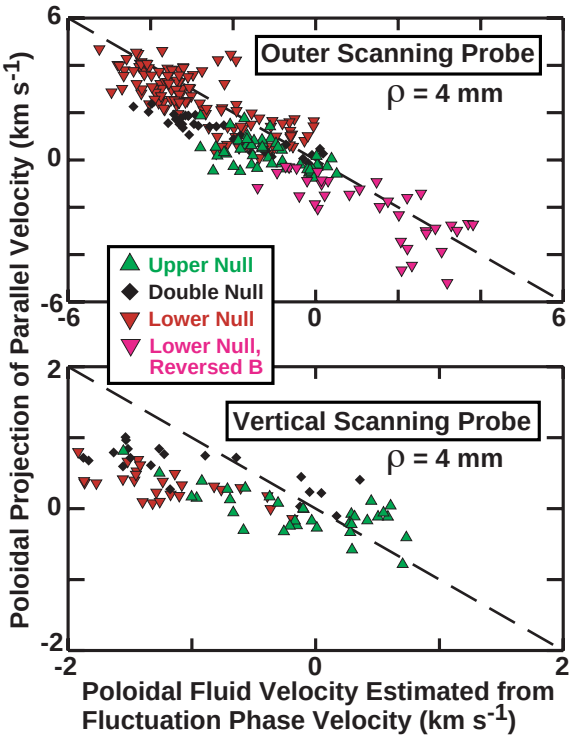

Figure 12. Poloidal projection of parallel flow versus poloidal fluid velocity estimated from fluctuation propagation, under the assumption that $\alpha = 1$ (see text). Positive velocity indicates a flow directed upwards. The dashed line corresponds to a condition of pure toroidal rotation.

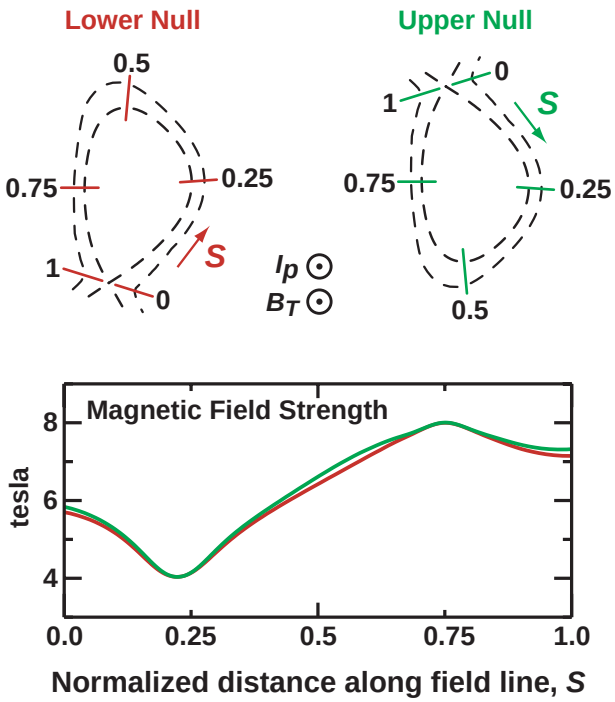

Figure 13. Definition of flux tube coordinate, s, in LSN and USN discharges. The flux surface shapes are similar when mirrored up/down, as shown by an overlay of magnetic field strengths from the $\rho = 4$ mm flux surface.

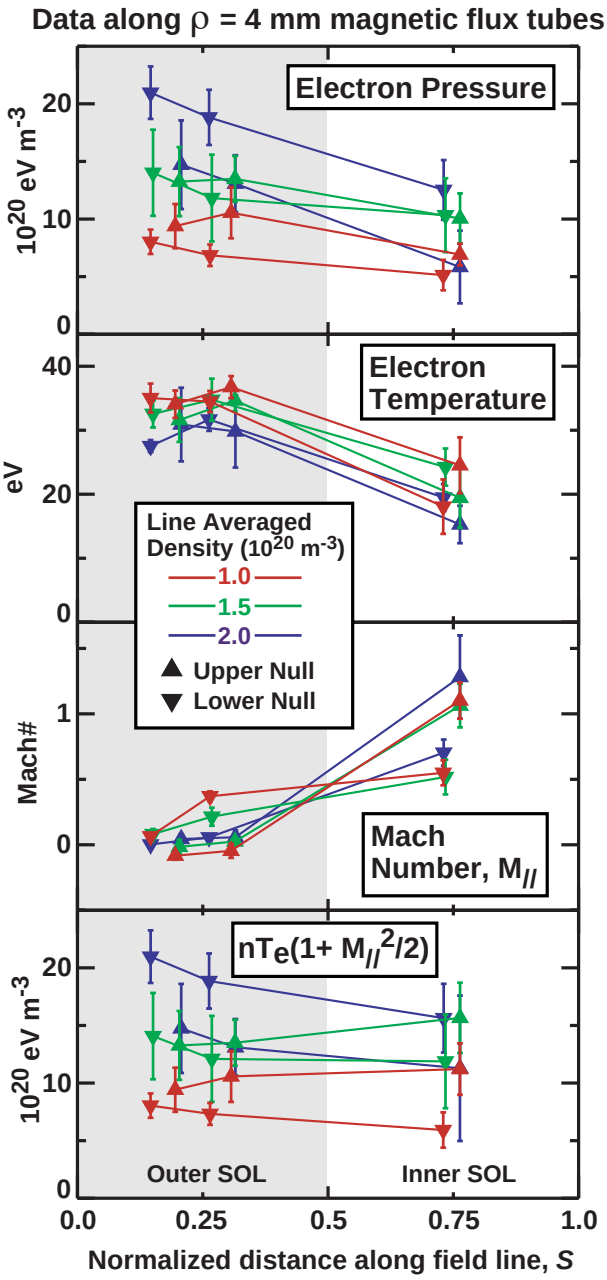

Figure 14. Plasma conditions at three scanning probe locations plotted versus flux tube coordinate, s, at the $\rho = 4$ mm flux surface. Straight lines connecting between symbols are included to guide the eye.

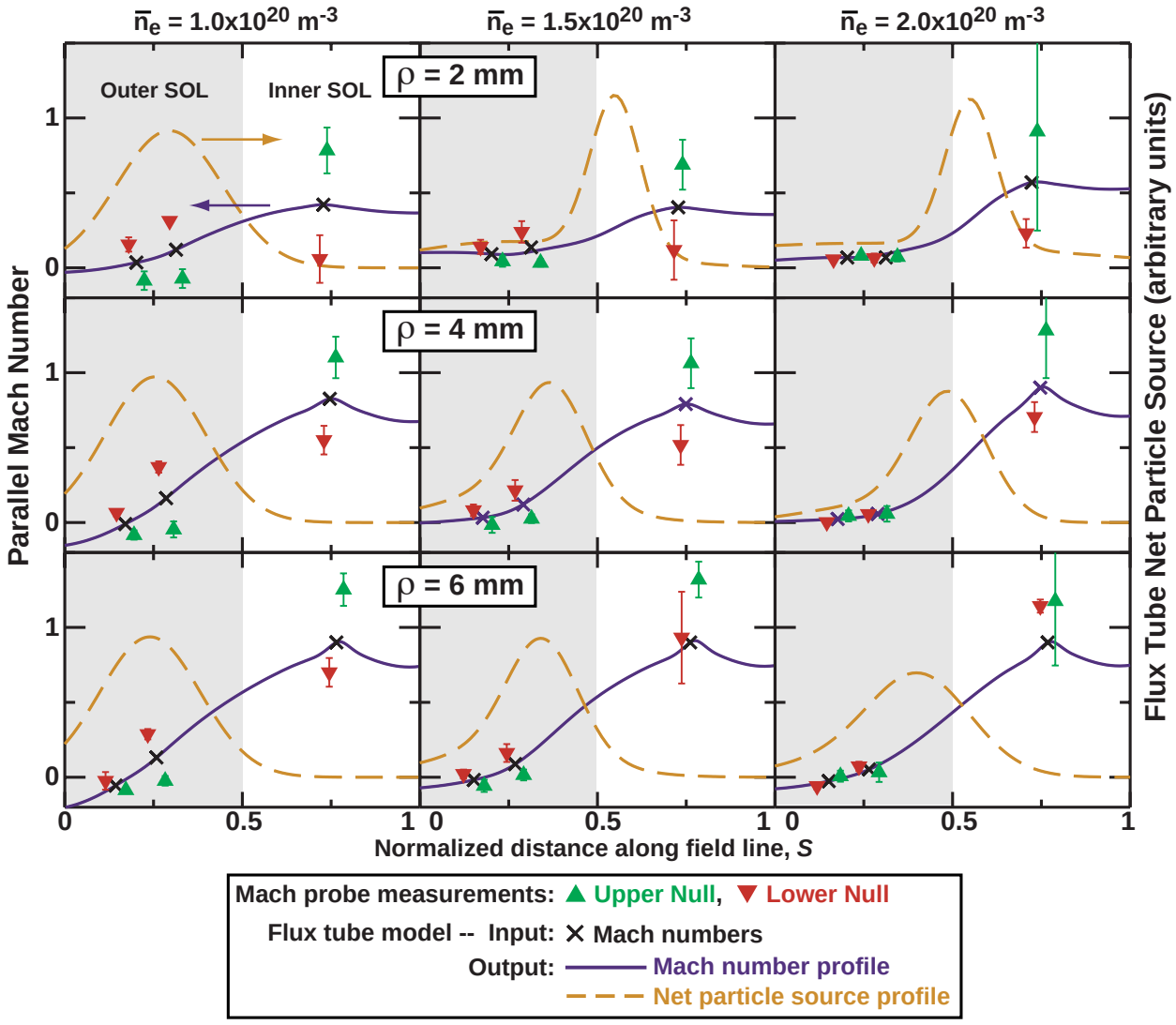

Figure 15. Results from parallel flow model (from same data set as Fig. 5).

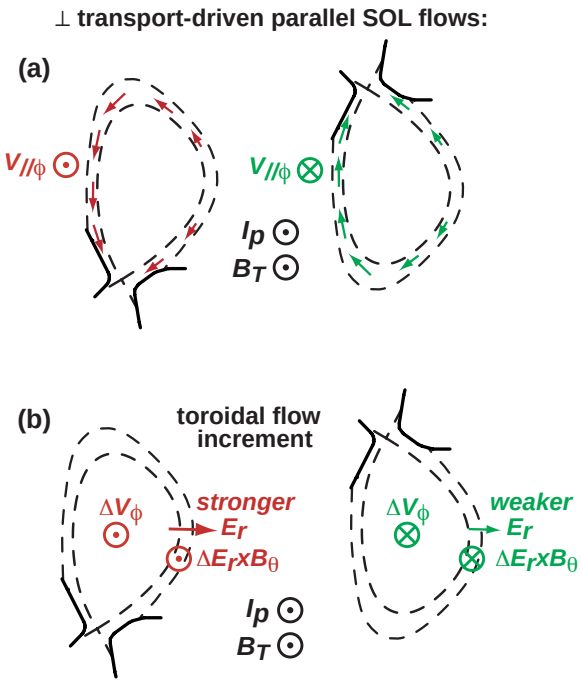

Figure 16. (a) Ballooning-like transport leads to a net volume-averaged SOL plasma momentum, co- or counter-current directed, depending on x-point location. (b) Data in Figs. 17 and 18 show that the confined plasma can react to this boundary condition with a positive (negative) increment in co-current rotation when $B \times \nabla B$ is towards (away from) the x-point. Correspondingly, toroidal rotation and radial electric fields in the SOL are influenced (as suggested from data in Fig. 11), becoming more (less) positive.

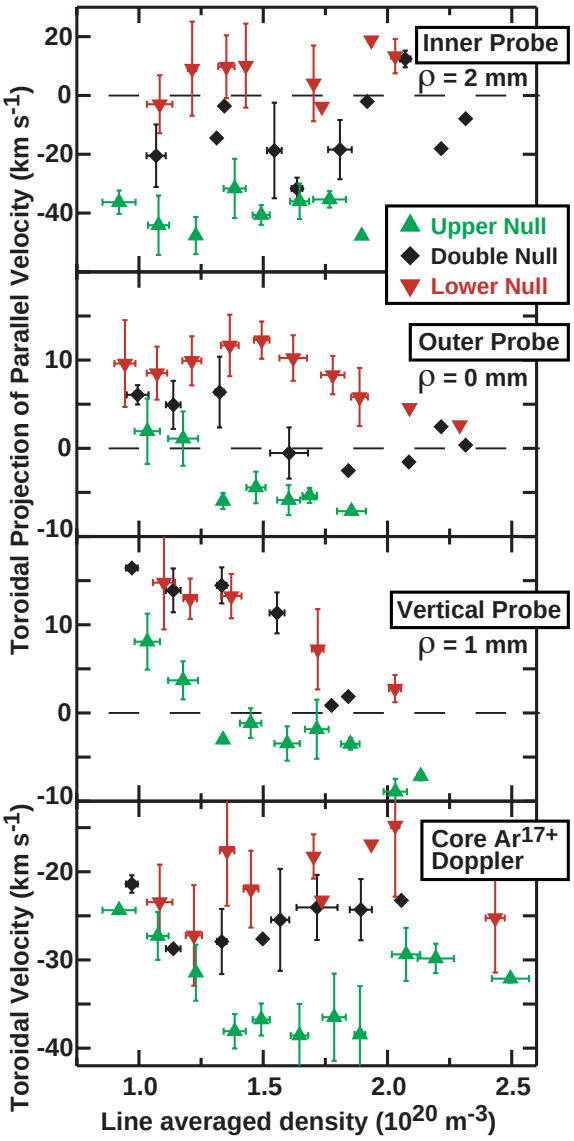

Figure 17. Toroidal projection of parallel plasma flow measured near separatrix by three scanning probes (top three panels) and corresponding toroidal velocity of central Ar^{17+} ions (bottom panel). In changing from upper to lower null, a positive increment in toroidal velocity (co-current directed) is detected on all signals. Data points are binned with $\Delta\bar{n}_e \sim 0.14 \times 10^{20}$ m^{-3}. Vertical bars indicate ±1 standard deviation.

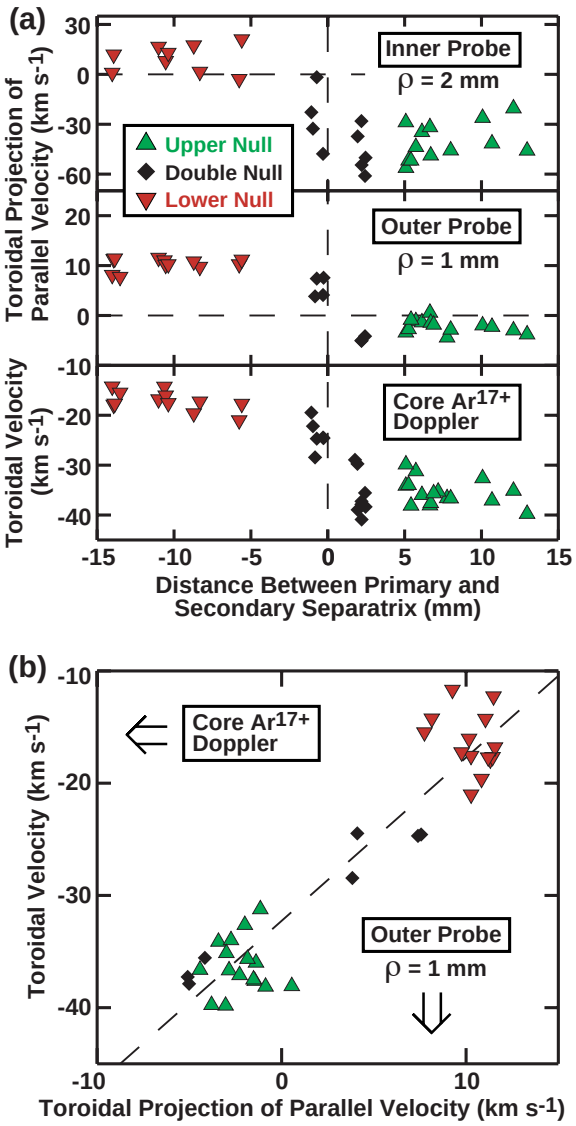

Figure 18. (a) Toroidal flow velocities as a function of magnetic flux balance between upper and lower x-point in otherwise identical discharges. (b) Toroidal velocity of central Ar^{17+} ions versus toroidal projection of parallel flow measured by the outer probe, at a location 1 mm outside the separatrix. The fitted dashed line has a slope of 1.5.

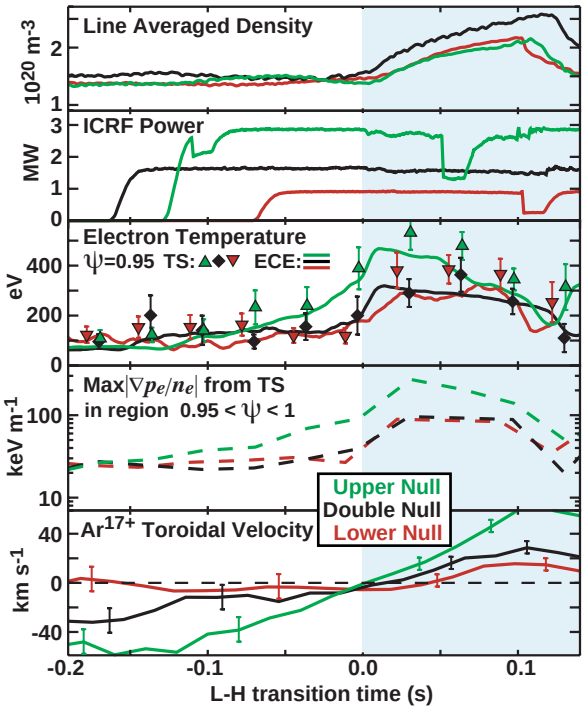

Figure 19. Time traces from LSN, DN, and USN discharges ($B \times \nabla B$ down) with nearly identical I_p B_T, and $\overline{n}_e$. ICRF power is applied to induce an L-H transition. The time axis is offset, placing zero near the time of transition. Edge electron temperatures are measured by electron cyclotron emission (ECE) and edge Thomson scattering (TS). Electron pressure gradients at the 95% flux surface are shown as dashed lines. The time of L-H transition is seen to coincide with central toroidal rotation (measured via Ar^{17+} Doppler) achieving roughly the same value (~0 km s^{-1} in this case), independent of magnetic topology. In contrast, USN edge electron temperatures and pressure gradients are clearly different than LSN.

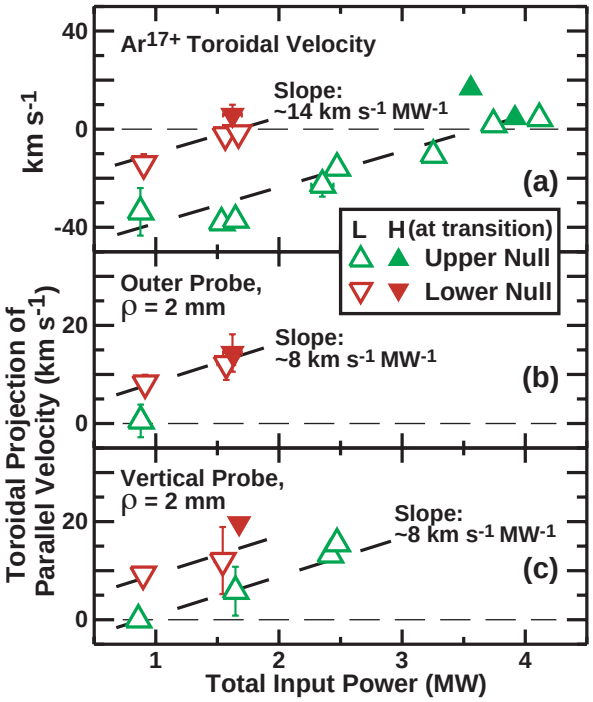

Figure 20. Toroidal velocities at the plasma center and 2 mm into the SOL as a function of total input power in otherwise identical plasmas (ohmic power level corresponds to leftmost data points). Magnetic topology and input power combine to affect central and edge toroidal velocities. The L-H transition is seen when central rotation achieves roughly the same value in these discharges.